

REPUBLIC OF TURKEY  
YILDIZ TECHNICAL UNIVERSITY  
GRADUATE SCHOOL OF SCIENCE AND ENGINEERING

**METAL MEASUREMENT OF FOSSIL GALAXY GROUPS:  
XMM-NEWTON DATA ANALYSIS OF NGC 6482**

**Emine Gülmez**

MASTER OF SCIENCE THESIS  
Department of Physics  
M.Sc. Program in Physics

Supervisor  
Asst. Prof. Dr. Murat Hüdaverdi

Co-supervisor  
Dr. François Mernier

February, 2023

**REPUBLIC OF TURKEY**  
**YILDIZ TECHNICAL UNIVERSITY**  
**GRADUATE SCHOOL OF SCIENCE AND ENGINEERING**

**METAL MEASUREMENT OF FOSSIL GALAXY GROUPS:  
XMM-NEWTON DATA ANALYSIS OF NGC 6482**

A thesis submitted by Emine Gülmez in partial fulfillment of the requirements for the degree of **MASTER OF SCIENCE** is approved by the committee on 06.02.2023 in Department of Physics, M.Sc. Program in Physics.

Asst. Prof. Dr. Murat Hüdaverdi  
Yildiz Technical University  
Supervisor

Dr. François Mernier  
NASA Goddard Space Flight Center,  
University of Maryland  
Co-supervisor

**Approved By the Examining Committee**

Asst. Prof. Dr. Murat Hüdaverdi, Supervisor  
Yildiz Technical University

\_\_\_\_\_

Prof. Dr. Serap Güneş, Member  
Yildiz Technical University

\_\_\_\_\_

Prof. Dr. E. Nihal Ercan, Member  
Bogazici University

\_\_\_\_\_

I hereby declare that I have obtained the required legal permissions during data collection and exploitation procedures, that I have made the in-text citations and cited the references properly, that I haven't falsified and/or fabricated research data and results of the study and that I have abided by the principles of the scientific research and ethics during my Thesis Study under the title of Metal Measurement of Fossil Galaxy Groups: XMM-Newton Data Analysis of NGC 6482 supervised by my supervisor, Asst. Prof. Dr. Murat Hüdaverdi. In the case of a discovery of false statement, I am to acknowledge any legal consequence.

Emine Gülmez

Signature

This study was supported by the Scientific and Technological Research Council of Turkey (TUBITAK) Grant No: 121F263.

*to everyone who contributed to me becoming who I am  
and who fought to make our "pale blue dot" a better place*

## ACKNOWLEDGEMENTS

---

I would like to express my deepest gratitude to my advisor, Asst. Prof. Dr. Murat Hüdaverdi, for their guidance, support, and encouragement throughout the entire process of this thesis. Their expert knowledge, invaluable feedback, and unwavering belief in me were essential in the completion of this work.

I would also like to extend my sincere appreciation to my co-advisers, Dr. François Mernier, for their invaluable contributions and for providing me with the opportunity to work with them. Their insights, expertise, and guidance have been instrumental in shaping my research. I would like to thank my laboratory partners M. Kiyami Erdim, Onur Ünver, Fatih Hazar, Burak Bektaşoğlu, Cemile Ezer, Ezgi Altıntaş, for their companionship, support, and for creating a positive and productive work environment. Their contributions to the lab and their willingness to share their knowledge have been greatly appreciated.

I would also like to thank my family, for their love, support, and understanding throughout the years. Their unwavering support and belief in me helped me through the most challenging times and motivated me to keep going. This thesis is as much a reflection of their love and support as it is of my own efforts. I would also like to thank my husband Hakan Necmettin Azman, for his patience and unwavering support, his encouragement and understanding, his help and his love throughout the years.

Finally, I would like to acknowledge the contributions of OpenAI's ChatGPT. The model helped me in finding papers that answers to some of my questions and provided me valuable information. It has been a great tool for me in my research.

I am truly grateful to everyone who has helped me in this journey and I couldn't have done it without you.

Emine Gülmez

# TABLE OF CONTENTS

---

<b>LIST OF SYMBOLS</b>	<b>viii</b>
<b>LIST OF ABBREVIATIONS</b>	<b>ix</b>
<b>LIST OF FIGURES</b>	<b>xi</b>
<b>LIST OF TABLES</b>	<b>xiii</b>
<b>ABSTRACT</b>	<b>xiv</b>
<b>ÖZET</b>	<b>xv</b>
<b>1 INTRODUCTION</b>	<b>1</b>
1.1 Literature Review . . . . .	1
1.1.1 Definition of Groups of Galaxies . . . . .	2
1.1.2 Classifying of Groups of Galaxies . . . . .	2
1.1.3 NGC 6482 Galaxy Group . . . . .	3
1.1.4 Intra-group Medium . . . . .	5
1.2 Objective of the Thesis . . . . .	5
1.3 Hypothesis . . . . .	6
<b>2 X-RAY EMISSION PROCESS IN THE INTRAGROUP MEDIUM</b>	<b>7</b>
2.1 The Continuum X-Ray Emission . . . . .	7
2.2 Line Emission . . . . .	8
<b>3 TRACE OF CHEMICAL ELEMENTS</b>	<b>10</b>
3.1 SN Explosions and Classification . . . . .	11
3.1.1 Core Collapse Supernovae . . . . .	12
3.1.2 Type Ia Supernova . . . . .	12
<b>4 THE XMM-NEWTON X-RAY TELESCOPE</b>	<b>14</b>
4.1 Components of XMM-NEWTON . . . . .	15
4.1.1 The Focal Plane Assembly . . . . .	15
4.1.2 Mirror Support Platform . . . . .	16
4.1.3 Telescope Tube . . . . .	16

4.1.4	Service Module . . . . .	16
4.2	The Orbit of XMM-Newton . . . . .	16
4.3	The Scientific Instruments of XMM-Newton . . . . .	17
4.3.1	EPIC Instruments . . . . .	18
<b>5</b>	<b>DATA REDUCTION AND ANALYSIS</b>	<b>20</b>
5.1	Data Reduction . . . . .	20
5.1.1	Observation . . . . .	20
5.1.2	Creating Cleaned Event Files . . . . .	20
5.1.3	Point Source Detection . . . . .	22
5.1.4	Creating Spectrum Files . . . . .	24
5.2	BACKGROUND ANALYSIS . . . . .	24
5.2.1	Noncosmic X-Ray Background . . . . .	24
5.2.2	Kozmik X-ray Background . . . . .	26
5.2.3	Background Modelling . . . . .	27
5.3	Source Analysis . . . . .	28
5.3.1	Astrophysical Plasma Emission Code . . . . .	28
5.3.2	Multi-temperature with Gaussian Distribution of Emission Measure . . . . .	28
<b>6</b>	<b>RESULTS AND DISCUSSION</b>	<b>29</b>
6.1	Temperature and Metal Distributions . . . . .	29
6.2	Discussion . . . . .	34
	<b>REFERENCES</b>	<b>38</b>

## LIST OF SYMBOLS

---

$D_A$	Angular diameter distance
'	Arcminute
"	Arcsecond
$\Delta m_{12}$	Absolute total magnitude gap in R band between the brightest and second brightest galaxies
AGB	Asymptotic Giant Branch
$L_{x,bol}$	Bolometric X-ray Luminosity
$k_B$	Boltzmann constant
erg	Erg
$\geq$	Greater than or equal
h	Hour
$h_{50}^{-2}$	Hubble Constant
$N_H$	Hydrogen Column Density
mag	Magnitude
Mpc	Megaparsec
$M_{\odot}$	Mass of Sun
$f_e(v)$	Maxwell-Boltzmann velocity distribution
$m_e$	Mass of the electron
m	Minute
s	Second
$Z_{\odot}$	Solar Metallicity
$T_{gas}$	Temperature of gas
$r_{vir}$	Virial radius

## LIST OF ABBREVIATIONS

---

APEC	Astrophysical Plasma Emission Code
APED	Astrophysical Plasma Emission Database
ARF	Ancillary Response File
CALDB	Calibration Database
CCD	Charge-Coupled Device
CfA	Centre for Astrophysics
CG	Compact Group
CGCG	Catalog of Galaxies and of Clusters of Galaxies
CXB	Cosmic X-ray Background
d.o.f	Degrees of freedom
EPIC	European Photon Imaging Camera
ESA	European Space Agency
FG	Fossil Group
GC	Cluster of Galaxies
GG	Groups of Galaxies
GH	Galactic Halo
HCG	Hickson Compact Galaxy Group Catalogue
ICM	Intracluster Medium
IGrM	Intragroup Medium
ISM	Interstellar Medium
LHB	Local Hot Buble
LMXB	Low Mass X-ray Binary
MRK	Markarian

NGC	New General Catalog
NXB	Noncosmic X-ray Background
ODF	Observation Data File
OGB	Outgassing Buffer
RASS	ROSAT All Sky Survey
RMF	Redistribution Matrix File
SN	Supernovae
SNIa	Type Ia Supernovae
SNcc	Core Collapse Supernova
SWCX	Solar Wind Charge Exchange
TSS	Telescope Sun Shield
UGC	Uppsala General Catalogue of Galaxies
VOD	Venting and Outgassing Doors
XSA	XMM-Newton Science Archive
z	Redshift

## LIST OF FIGURES

---

<b>Figure 1.1</b>	The Schematic Diagram of GG Classification: Diagram showcasing the galaxy group classification scheme, displaying the different types of galaxy groups such as compact groups, loose groups, and fossil groups in terms of their space density. . . . .	3
<b>Figure 1.2</b>	The image of the identified members of NGC 6482 Group in optical range: The image shows the NGC 6482 galaxy group and its members with their brightness and distribution. ( <i>ALADIN: Astronomical Atlas and Data Image Server</i> n.d.) . . . . .	4
<b>Figure 2.1</b>	The comparison of X-ray emission spectra of hot plasma at different temperatures (Böhringer 2014) . . . . .	9
<b>Figure 3.1</b>	Classified Supernova Types Schematic Overview ( <i>COSMOS - The SAO Encyclopedia of Astronomy: Supernova Classification</i> n.d.) . . .	11
<b>Figure 4.1</b>	Artist’s portrayal of the XMM-Newton ( <i>ESA: XMM-Newton Operations</i> n.d.) . . . . .	14
<b>Figure 4.2</b>	The Physical Composition of XMM-Newton Telescope including X-Ray Mirror Assemblies and Focal Plane Cameras located at both ends of the Telescope Tube. (Barré, Nye, Janin 1999) . . . . .	15
<b>Figure 4.3</b>	The Schematic View of XMM-Newton Orbit ( <i>HEASARC: XMM-Newton Mission Orbit</i> n.d.) . . . . .	17
<b>Figure 4.4</b>	The Scientific Instruments of XMM-Newton Orbit with 3 EPIC Camera (2 MOS and 1 PN), 2 RGS Camera and an Optical Monitor ( <i>ESA: XMM-Newton Payload</i> n.d.) . . . . .	18
<b>Figure 4.5</b>	The Sketch of EPIC MOS (left) and EPIC PN (right) CCDs arrays. The circle with shading represents a 30’ diameter region. ( <i>ESA: EPIC CCDs</i> n.d.) . . . . .	19
<b>Figure 5.1</b>	MOS1 (left), MOS2 (middle) and PN (right) Images with created <i>mos-filter</i> and <i>pn-filter</i> task . . . . .	21
<b>Figure 5.2</b>	Light Curves of MOS1 (top), MOS2 (middle) and PN (bottom) . .	22
<b>Figure 5.3</b>	EPIC (MOS and PN) combined image: yellow circles are symbolized detected regions of point sources with Chandra <i>wavdetect</i> task . . .	23

<b>Figure 5.4</b>	MOS1 (left), MOS2 (middle) and PN (right) cheese images created with <i>make_mask</i> . . . . .	23
<b>Figure 5.5</b>	EPIC combined and cleaned point sources image of NGC 6482 . .	24
<b>Figure 5.6</b>	The image illustration of the local hot bubble ( <i>NASA, Local Hot Bubble</i> n.d.) . . . . .	26
<b>Figure 6.1</b>	EPIC spectra of 0-20 arcsec region of NGC 6482 . . . . .	30
<b>Figure 6.2</b>	EPIC spectra of 20-50 arcsec region of NGC 6482 . . . . .	31
<b>Figure 6.3</b>	EPIC spectra of 50-90 arcsec region of NGC 6482 . . . . .	32
<b>Figure 6.4</b>	EPIC spectra of 90-140 arcsec region of NGC 6482 . . . . .	33
<b>Figure 6.5</b>	The derived radial temperature profile is shown. The indicated temperature here demonstrates the mean temperature of the plasma and the red vertical lines presents the sigma temperature. .	35
<b>Figure 6.6</b>	The derived and compared radial Fe, Si, Mg and S profile is shown.	36

## LIST OF TABLES

---

<b>Table 1.1</b>	NGC 6482 Group Members: The known members of the galaxy group NGC 6482, along with their coordinates (J2000) and total B-magnitudes in unit mag . . . . .	4
<b>Table 4.1</b>	The XMM-Newton Orbit Parameters . . . . .	16
<b>Table 5.1</b>	Observation information of the NGC 6482 from the XMM-Newton data archive . . . . .	20
<b>Table 5.2</b>	EPIC Cameras and Their Cleaned Exposures . . . . .	22
<b>Table 6.1</b>	Best fit <i>vgadem</i> model parameters with $1\sigma$ errors for 0-20 arcsec region of NGC 6482 . . . . .	30
<b>Table 6.2</b>	Best fit <i>vgadem</i> model parameters with $1\sigma$ errors for 20-50 arcsec region of NGC 6482 . . . . .	31
<b>Table 6.3</b>	Best fit <i>vgadem</i> model parameters with $1\sigma$ errors for 50-90 arcsec region of NGC 6482 . . . . .	32
<b>Table 6.4</b>	Best fit <i>vgadem</i> model parameters with $1\sigma$ errors for 20-50 arcsec region of NGC 6482 . . . . .	33
<b>Table 6.5</b>	Best fit <i>vgadem</i> model parameters of abundance with $1\sigma$ errors for all four annuli . . . . .	34

# Metal Measurement of Fossil Galaxy Groups: XMM-Newton Data Analysis of NGC 6482

Emine Gülmez

Department of Physics  
Master of Science Thesis

Supervisor: Asst. Prof. Dr. Murat Hüdaverdi

Co-supervisor: Dr. François Mernier

Galaxy groups are structures that comprising more than half of all galaxies. They have hot ( $10^7$  K) intra-group medium (IGrM) that emit X-rays and exhibit numerous emission lines of elements synthesized by stars and during supernovae. Galaxy groups have lower gravitational potentials compared to rich galaxy clusters and the difficulty of detecting them optically. Therefore X-ray observations which carries significant signatures about metal content provide an ideal means for studying galaxy groups.

In this study, we aimed to identify elements dispersed into the environment by supernovae by examining the hot plasma surrounding the member galaxies of the nearest known fossil galaxy group, NGC6482 ( $z\sim 0.012$ ), using observations ( $\sim 142$  ks) from the European Photon Imaging Camera (EPIC) of the XMM-Newton satellite sent into its operational orbit by the European Space Agency (ESA). We measured the abundance of Fe, Mg, Si, and S elements in the NGC 6482's IGrM. We discussed the implications of the element ratios and amounts in relation to the Fe element.

**Keywords:** Fossil Group, NGC6482, Metal Abundance, Chemical enrichment, Galaxy Groups, XMM-Newton

# Fosil Galaksi Gruplarının Metal Ölçümü: NGC 6482'nin XMM-Newton Veri Analizi

Emine Gülmez

Fizik Anabilim Dalı

Yüksek Lisans Tezi

Danışman: Dr. Öğr. Üyesi Murat Hüdaverdi

Eş-Danışman: Dr. François Mernier

Galaksi grupları tüm galaksilerin yarısından fazlasını oluşturan yapılardır. X-ışınları yayan Sıcak ( $10^7$  K) grup içi ortamları (IGrM), yıldızlar tarafından ve süpernova patlamaları sırasında sentezlenen çok sayıda elementi gösteren emisyon çizgilerine sahiptir. Zengin galaksi kümelerine göre daha az derin kütleçekimsel potansiyelleri ve optik olarak tespit edilmelerinin zorluğu sebebiyle, galaksi grupları metal içeriğiyle ilgili önemli izler taşıyan X-ışınları gözlemleriyle çalışmak için idealdir.

Bu çalışmada, bilinen en yakın ( $z \sim 0.012$ ) fosil galaksi grubu olan NGC 6482'nin grup üyesi galaksilerini saran sıcak plazmayı inceleyerek, süpernova patlamalarından kaynaklı ortama saçılmış olan elementleri Avrupa Uzay Ajansının (ESA) fırlattığı XMM-Newton uydusunun Avrupa Photon Görüntüleme Kamera (EPIC) gözlemini ( $\sim 142$  ks) kullanarak tespit etmeye çalıştık. Fe, Mg, Si ve S elementlerini ölçerek NGC 6482'nin IGrM'indeki bolluk miktarlarını tespit ettik. Element miktarlarının ve elementlerin Fe elementine oranlarını tartıştık.

**Anahtar Kelimeler:** Fosil Grup, NGC6482, Metal Bolluk, Kimyasal Zenginleşme, Galaksi Grupları, XMM-Newton

# 1

## INTRODUCTION

---

### 1.1 Literature Review

The history of the exploration of astronomical objects is detailed in the work "From Messier to Abell: 200 Years of Science With Galaxy Clusters" by Andrea Biviano (Biviano 2000). In this section, we will provide a brief overview of galaxy groups based on the information provided in this study.

The identification and study of galaxy groups and galaxy clusters (hereafter GG and GC respectively) began in the early 1900s through the research of astronomers like George Abell. Abell's publication "The Distribution of Rich Clusters of Galaxies" marked a significant achievement in this field. Despite this, many thousands of GCs and GGs went uncatalogued due to their lack of sufficient richness to guarantee their full identification.

The field of GGs saw early progress with the publication of a list of 55 GGs by de Vaucouleurs, which was based on his Reference Catalogue. This was subsequently followed by the publication of a list of 174 GGs by Holmberg. In 1977, a catalogue of compact galaxies are published by Shakhbazyan and Petrosyan and Rose published a catalogue of compact groups (hereafter CG). The first complete catalogue of CG was provided by Turner and Gott in 1978.

The Center for Astrophysics (CfA) Redshift survey was the a catalog of GG published by Huncra and Galler. It was the initial significant accomplishment and first identification of GGs in 3-D space with describing volume-density improvements in the distrubution of galaxies. There were 176 GC in the catalog and 74 of them being newly found.

Simultaneously, Hickson Compact Galaxy Group Catalogue (HCG) also published by Hickson. The catalogue included 100 CGs. The early catalogs that were discovered represented a significant advancement in understanding the importance of GGs and their role in the large-scale structure of the universe.

Following that, Bhavsar and de Souza continued to examine the morphology-density relation by studying loose groups of galaxies. They expanded the research into the low galaxy density regime by analyzing GGs that have fewer galaxies in comparison to rich GCs.

In 1981, Carnevali presented a model for the evolution of small GGs. They proposed that the "merging instability" leads to the formation of a large central object in these groups. This model was particularly noteworthy as it anticipated the later discovery of a class of GGs known as "fossil groups" (Hereafter FG) which have a large central galaxy surrounded by a small number of satellites. This discovery was made by Ponman in the following years. Despite ongoing research, GGs remain a topic of ongoing mystery and study.

### 1.1.1 Definition of Groups of Galaxies

Galaxies are collections of stars that are bound together by gravity. The formation of galaxies is thought to occur through the gravitational collapse of gas clouds. When galaxies come together, they can form GGs and GCs. These structures are characterized by their mass, with GGs generally having lower masses ( $10^{13}$ – $10^{14}M_{\odot}$ ) than GCs ( $10^{14}$ – $10^{15} M_{\odot}$ ) (Lovisari et al. 2021) , (Voit 2005). However, we don't have a identification universally accepted for GGs. The difference between GG and GC is not always clear but in general, GGs are defined as systems containing fewer than 50 galaxies, while GCs are defined as systems containing more than 50 galaxies (Lovisari et al. 2021). They can be divided into three major categories based on their properties in physical and optical(Eigenthaler, Zeilinger 2007).

### 1.1.2 Classifying of Groups of Galaxies

The classification of GGs, as seen in the 1.1, is as follows: compact groups, poor or loose groups, and fossil groups.

As the name implies, small collections of several galaxies that are closely situated in relation to one another in the sky are referred to as compact groups of galaxies (Hickson 1997). The first systematic study of these properties was published by Hickson in 1982 (Hickson 1982). Within each group in the HCG, four or more galaxies are present within a 3 magnitude range of the brightest galaxy. The HCG groups has also an isolation criterion and the mean surface brightness was also estimated by exceeding 26.0 mag arcsec<sup>2</sup>. The space density of CG is about  $\sim 1-2 \times 10^{-6} \text{ Mpc}^{-3}$ .

A majority of collections of galaxies are classified as loose associations. Loose or poor

groups, are the most prevalent type of GGs. They have a space density of around  $10^{-5} \text{ Mpc}^{-3}$  and exhibit similar characteristics to simple multiplets of galaxies. They tend to have diameter of about 1.5 Mpc (Nolthenius, White 1987).

Loose or poor GGs can evolve into FGs (Eigenthaler, Zeilinger 2007). FGs have also  $\sim 1-4 \times 10^{-6} \text{ Mpc}^{-3}$  space density (La Barbera et al. 2009). The definition of FGs for the first time is given by (L. Jones et al. 2003). Their definition is as follows "A fossil system in observational terms as a spatially extended X-ray source with an X-ray luminosity from diffuse, hot gas of  $L_{X,bol} \geq 10^{42} h_{50}^{-2} \text{ ergs}^{-1}$ . The optical counterpart is a bound system of galaxies with  $\Delta m_{12} \geq 2.0$  mag, where  $\Delta m_{12}$  is the absolute total magnitude gap in R band between the brightest and second brightest galaxies in the system within half the (projected) virial radius ( $r_{vir}$ )."

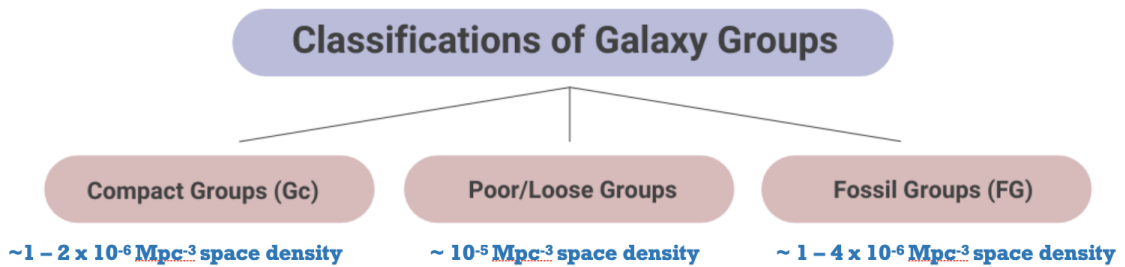


**Figure 1.1** The Schematic Diagram of GG Classification: Diagram showcasing the galaxy group classification scheme, displaying the different types of galaxy groups such as compact groups, loose groups, and fossil groups in terms of their space density.

### 1.1.3 NGC 6482 Galaxy Group

NGC 6482 is the known nearest ( $z \sim 0.012$ ) GG classified as a FG, characterized by the dominance of a single, NGC 6482, optically luminous giant elliptical galaxy which is among the largest known galaxy types at the core of the group (*NED: NASA/IPAC Extragalactic Database* n.d.). The group is known to have only a few other confirmed members within a radius of  $60'$  from the brightest galaxy, as observed by their relative magnitudes, which are more than 2 magnitudes fainter than NGC 6482 (Khosroshahi, Laurence R Jones, Ponman 2004). These members include UGC 11024, UGC 11018, CGCG 141-014 and MRK 895 galaxies.

In figure 1.2 NGC 6482 and its confirmed group members are displayed in optical range. This image provides a visual representation of the galaxy group and offers insights into the distribution of other members and their brightness within the group. Additionally, the coordinates and magnitudes of the individual members are exhibited in table 1.1. There is approximately a 2 magnitude difference between the brightness of the brightest galaxy and the second brightest galaxy. The image showing NGC

6482 GG with its members were created with Aladin Sky Survey (*ALADIN: Astronomical Atlas and Data Image Server* n.d.). The coordinates and magnitudes values are in the table were taken from NASA/IPAC Extragalactic Database and HYPERLEDA respectively (*NED: NASA/IPAC Extragalactic Database* n.d.), (*HyperLeda: Database for physics of galaxies* n.d.).

Studying GGs like NGC 6482 can give us a deeper understanding of how large scale structures, such as GCs and superclusters, form and evolve over time in the universe.

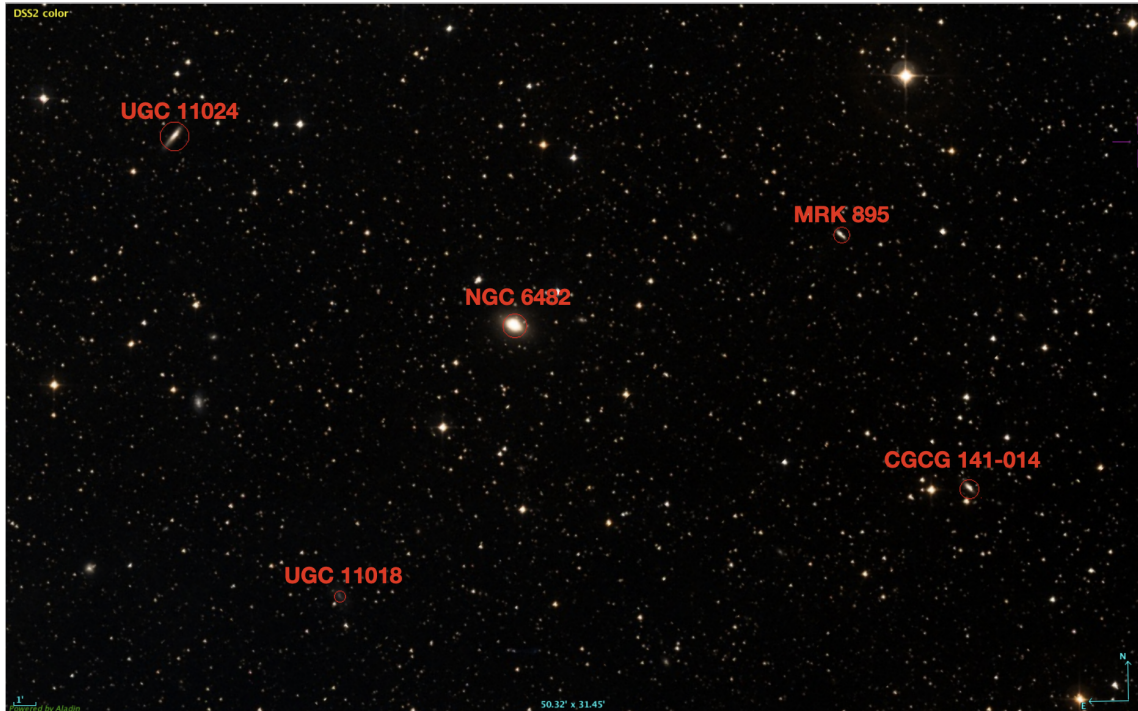


**Figure 1.2** The image of the identified members of NGC 6482 Group in optical range: The image shows the NGC 6482 galaxy group and its members with their brightness and distribution. (*ALADIN: Astronomical Atlas and Data Image Server* n.d.)

**Table 1.1** NGC 6482 Group Members: The known members of the galaxy group NGC 6482, along with their coordinates (J2000) and total B-magnitudes in unit mag

Members	Right Ascension (RA)	Declination (Dec)	Total B-magnitude (mag)
NGC6482	17h51m48.81s	+23d04m19.0s	12.23
UGC 11018	17h52m22.38s	+22d52m19.5s	17.00
MRK 895	17h50m45.77s	+23d08m19.0s	15.10
UGC 11024	17h52m54.49s	+23d12m39.8s	14.94
CGCG 141-014	17h50m21.220s	+22d57m04.60s	15.30

#### **1.1.4 Intra-group Medium**

GGs have received less attention despite playing a fundamental role in the formation and evolution of the cosmic structure. One of the reasons for this is that typical GGs typically only contain one or a few bright galaxies in their central regions, which makes them difficult to detect optically. However, thanks to the technology of developing X-ray telescopes, it is now known that GGs contain spatially extended X-ray emission. This X-ray emission is caused by the presence of a diffuse, low-density gas component known as the Intragroup medium (IGrM). The IGrM is a dispersed, dilute gas found in the space between galaxies within a GG, and the X-ray emission from the IGrM allows for the study of GGs.

Studies on element abundance measurements are quite popular in GCs, which have a hierarchical position over GGs and provide important information for understanding the universe. However, studies in this area are quite limited in GGs. Through X-rays emitted by IGrM, metal measurements can be made, and this metal content can give an idea about the star formation and galaxy mergers within the group, as well as how galaxies formed and evolved in these environments.

Studies of metal abundance in IGrMs in the literature are limited, but several notable ones include (Mulchaey 2000) which provides information about the early history of such measurements, (Sato et al. 2010) which studied the temperature and metal abundance distribution in NGC 1550, (Sun 2012) which examined Chandra and XMM-Newton data on hot gas in GGs, (Mernier et al. 2018) which compared the metal budget between GGs and GCs, (Dupke et al. 2022) which examined the metal abundance gradient in RX J100742.53+380046.6, and (Sarkar et al. 2022) which presents Fe, Mg, O, S, and Si abundances for four nearby GGs on their outskirts.

Based on all the limited studies and the information obtained, in this study, we will measure the metals in the hot IGrM of the fossil group NGC 6482 and interpret where they came from. This study is unique because it is one of the few studies on chemical enrichment in fossil GGs and it is the first detailed examination of NGC 6482 from this perspective.

## **1.2 Objective of the Thesis**

Despite constantly gaining new knowledge about the universe, there still remain many unresolved and debated topics. Examining large structures in the universe, such as galaxy groups, can provide insight into our understanding of it. The aim of this thesis is to analyze X-ray emissions from groups of galaxies, which carry important information about the groups, using X-ray observations. The ultimate goal is to gain

new knowledge that will contribute to our overall understanding of the universe.

### **1.3 Hypothesis**

The hypothesis of this thesis is that the metal content within NGC 6482, a fossil group of galaxies, can be effectively studied through X-ray observations using the XMM-Newton satellite. The study will focus on NGC 6482 as an important and suitable sample due to its long observation period and the limited number of studies on the abundance of elements in fossil groups. In summary, it is expected that XMM-Newton data will provide valuable information on the distribution of elements within NGC 6482 and offer new insights into the chemical enrichment relationships of fossil groups.

# 2

## X-RAY EMISSION PROCESS IN THE INTRAGROUP MEDIUM

---

GGs generally have lower and flatter X-ray surface brightness than GCs (Ponman, Cannon, Navarro 1999), (Sanderson et al. 2003). Therefore, the X-ray emissions emitted by GGs and GCs have different signatures. There are two well-known differences between X-rays emitted from the ICM and those emitted from the IGrM.

The first difference between the ICM and IGrM is that while the dominant X-ray mechanism in the ICM is free - free bremsstrahlung due to its high temperature, the IGrM, with an average temperature of 1 keV, also has contributions from radiative recombination (free-bound) and two photon emission (bound-bound processes) that affect the continuum level (Mewe, Lemen, Van den Oord 1986), (Böhringer, Werner 2010).

Another distinction between the ICM and IGrM is linked to temperature. When temperatures rise (about 4 keV and above), the dominant line emission is from the Fe-K line. However, when temperatures fall below 2 keV, the primary line emission shifts towards the Fe-L line.

### 2.1 The Continuum X-Ray Emission

The primary mechanisms for the production of continuum emission are thermal bremsstrahlung (free-free emission), radiative recombination with free-bound transition, and emission of two photons through bound-bound transitions (Sarazin 1988).

Thermal bremsstrahlung, also known as free-free emission, is the primary mechanism for the production of continuum emission in hot, diffuse gas. It is characterized by the emission of electromagnetic radiation as charged particles are decelerated by interactions with other charged particles. This type of emission is typically associated

with high temperatures, as it is produced by a hot, diffuse gas that is assumed to be at a uniform temperature and follows a Maxwell-Boltzmann velocity distribution.

$$f_e(v) \propto \exp\left(\frac{-m_e v^2}{2k_B T_{gas}}\right) v^2 dv \quad (2.1)$$

where  $k_B$  represents the Boltzmann constant,  $m_e$  stands for the mass of the electron, and  $T_{gas}$  is the temperature of gas.

Due to the relatively low temperature of IGrM ( $\sim 1$  keV), radiative recombination and two-photon emission mechanisms also make significant contributions to the X-ray radiation emitted by it.

Radiative recombination is a process in which a free electron combines with an ion to form a neutral atom, emitting a photon in the process. This mechanism, also known as free-bound emission, is characterized by the transition of a free electron to a bound state within an atom.

Two-photon emission is a mechanism in which a photon is emitted as a result of the simultaneous transition of two bound electrons within an atom or molecule. This process takes place when an electron in an excited state of 2s is unable to directly transition down to the 1s state due to it being forbidden, but it becomes more probable in gas with low density and ionization. As a consequence, the electron moves from the 2s to the 1s orbit by releasing two photons.

## 2.2 Line Emission

X-ray radiation in plasmas is largely produced through line emission, especially at lower temperatures. It is produced when an electron transitions between two different energy states, and is characterized by the emission of a specific spectrum of X-ray radiation. This radiation can be used to detect the abundance of different metals in a plasma, as each metal has a unique spectrum. By analyzing the line emission from a plasma, it is possible to determine the relative concentrations of different metals present. This is because each metal emits a distinct set of spectral lines at specific wavelengths, which can be used to identify it.

The most important emission line in the X-ray spectra of GCs is known as Fe-K. The first discovery of Fe-K emission was made in the Perseus cluster and it has been observed in many GCs since then (Mitchell et al. 1976). However, X-ray spectra can change as the temperature of the plasma changes. For example, the temperature of the IGrM is around 1 keV therefore, the Fe-K emission line is replaced by the Fe-L emission line.

Also, this is not only valid for the iron element, emission lines from other elements can also change. For example, Figure 2.1 compares two X-ray spectra at different temperatures (Böhringer 2014).

This figure presents a comparison of X-ray spectra from plasmas containing sun-like element abundances, one at  $10^7$  K on the left and the other at  $10^8$  K on the right. These spectra have been theoretically calculated and depicted using blue lines for Bremsstrahlung, green lines for recombination continuity, and red lines for two-photon emission. Additionally, the thick red lines on top of the figures indicate the roughly, spectral range encompasses by the XMM-Newton and Chandra detectors.

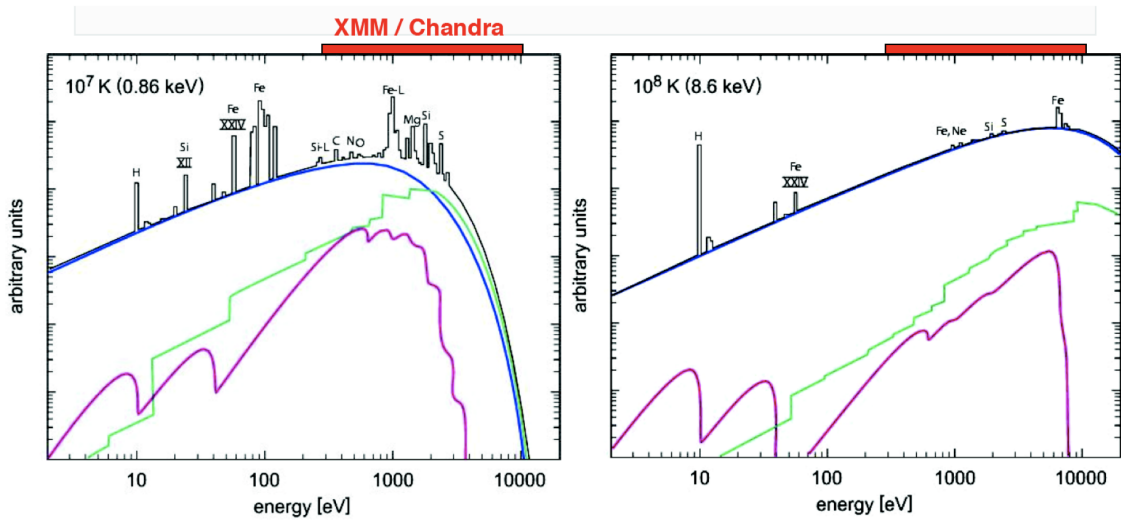


**Figure 2.1** The comparison of X-ray emission spectra of hot plasma at different temperatures (Böhringer 2014)

# 3

## TRACE OF CHEMICAL ELEMENTS

---

There are many important discoveries that suggest ways to search for the traces of chemical elements. Stars synthesize heavy elements through the process of nucleosynthesis. Nucleosynthesis occurs in the cores of stars and during supernovae (hereafter SN) explosions. As a result, the interstellar medium is enriched with new elements. This is one of the important discoveries and it excludes elements formed by primordial nucleosynthesis.

The lightest two elements, hydrogen and helium, were created shortly after the Big Bang (Gamow 1946). When the universe cooled down enough, protons and neutrons were able to form from quarks and some of them combined to form helium nuclei. This is known as primordial nucleosynthesis and is one of the key observations that supports the Big Bang theory.

Other elements (to a certain level of Li : Lithium, Be: Beryllium and B: Boron) are formed through nuclear fusion, such as the fusion of heavy elements in high-energy cosmic rays. Heavier elements are produced by stars and stellar remnants. In the core of stars, H: Hydrogen atoms (2 protons) are converted to He: Helium due to the extremely high temperatures. The mass of the newly formed He (2 protons) is actually less than what it should be (2 protons + 2 neutrons). The mass excess here corresponds to the energy produced during thermonuclear fusion. This energy produced keeps the star in hydrostatic equilibrium against its own gravitational pull. When the energy provided by H fusion weakens against the gravitational pull, heavier elements are synthesized (CNO cycle) through  $\alpha$  process.

From this point forward, the destiny of stars is determined by their mass (Clayton 1983). Stars with a mass less than eight times that of the sun ( $\lesssim 8M_{\odot}$ ) are classified as low to intermediate-mass stars. Those with a mass greater than ten times that of the sun ( $\gtrsim 10M_{\odot}$ ) are classified as high-mass stars.

C: Carbon, N: Nitrogen, and to a certain degree of Li are produced in

intermediate-mass stars and particularly in the final stages of their life by asymptotic giant branch (AGB) stars. The SN explosions of low and intermediate-mass stars of type Ia (hereafter SNIa) produce Fe-group elements (from Cr to Ni) and lighter elements (from Si to Ca).  $\alpha$  elements (elements produced by the alpha process that mentioned above; from O: Oxygen to Ca: Calcium) are produced by SN explosions that occur in high-mass stars and collapsing cores (hereafter SNcc) (François Mernier, Biffi 2022). In this study, we will focus on the dominant role of SNcc and SNIa supernova explosions in the synthesis of chemical elements and discuss details of SNcc and SNIa.

### 3.1 SN Explosions and Classification

When a star reaches the end of its life, a SN occurs. It is a powerful explosion and characterized by an intense release of energy. This event is among the brightest that can be observed and the energy released. The material that is ejected from the star during the explosion contains synthesized heavy elements. The chemical composition of this material is heavily influenced by the star that produced it (called the progenitor star), and the type of SN explosion that has occurred can be identified by examining certain elements. The classification of supernova explosions is based on the specific chemical elements present in their spectra (Turatto 2003).

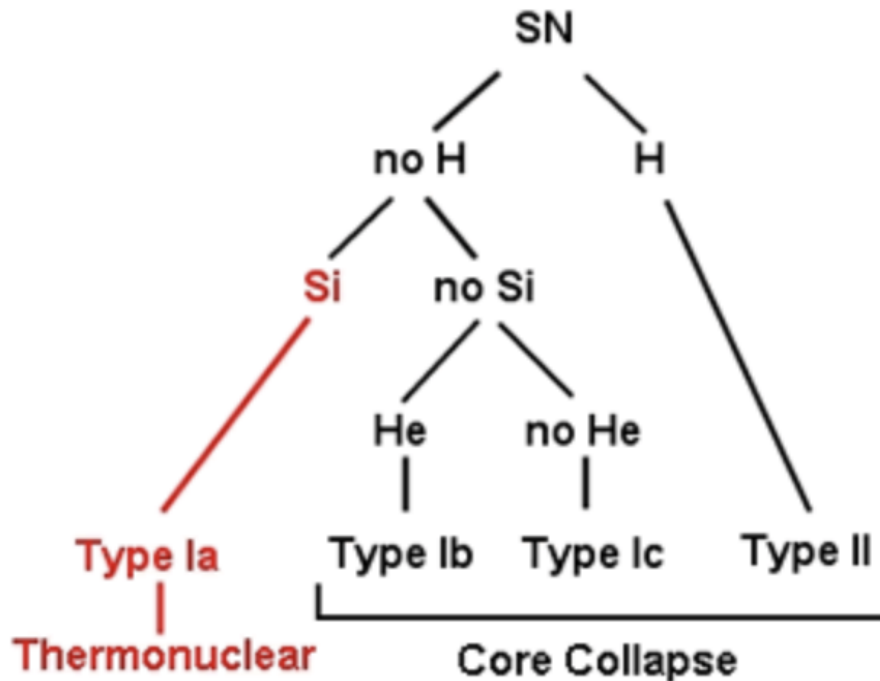


**Figure 3.1** Classified Supernova Types Schematic Overview (*COSMOS - The SAO Encyclopedia of Astronomy: Supernova Classification* n.d.)

SN are classified into two main categories based on H lines in the spectrum. Type I supernovae can be distinguished by the absence of hydrogen lines in their spectra, while the presence of hydrogen lines is used as a means of identifying Type II supernovae.

Each of these categories has been further divided into subcategories thanks to the advancement of scientific observations. SN I are divided into three subclasses: SN Ia, which are rich in silicon (Si) and characterized by Si absorption lines; SN Ib, which are rich in non-ionized helium (He) and characterized by He absorption lines; and SN Ic, which do not exhibit Si or He absorption lines.

### **3.1.1 Core Collapse Supernovae**

When core density of a massive star attain to the  $1.4 M_{\odot}$  also referred as Chandrasekhar limit, the pressure exerted by its electrons, the core can no longer be held up against the force of gravity by the pressure from its electrons, known as electron degeneracy pressure. This causes the protons in the core to capture electrons, creating neutrons and neutrinos. When the pressure from the neutrons, known as neutron degeneracy pressure, becomes strong enough to counterbalance the force of gravity, the contraction of the core ceases. This sudden halt in contraction generates a powerful shock wave that travels through the upper layers of the star at speeds of 25-50% the speed of light. The shock wave heats the material in these layers, causing the synthesis of elements such as oxygen, neon, and magnesium. These elements are also produced inside stars before SN, but they are consumed during the supernova process. Most of the oxygen, neon, and magnesium in the universe, as well as half of the silicon and sulfur, is produced by a specific type of supernova called a core-collapse supernova (SNcc) (Woosley, Janka 2005). Heavier elements such as calcium, argon, iron, and nickel may also be synthesized during an SNcc, but in smaller quantities.

Type I and Type II supernovae are associated with SNcc. Hydrogen being present in their spectra identifies Type II supernovae. Similarly, Type Ib and Type Ic, SNcc are also thought to have a connection to.

Type Ib and Type Ic SN are also thought to be related to SNcc, but they differ in that their hydrogen and helium layers have been lost, respectively.

### **3.1.2 Type Ia Supernova**

Type Ia supernovae are theorized to be caused by the thermonuclear ignition of a white dwarf star. These SN are believed to occur in binary star systems has a white

dwarf and companion star. A white dwarf gains material from its companion star and becomes unstable (Andrew Howell et al. 2006). The exact mechanism behind these explosions is not fully understood, but it is thought to involve the ignition of carbon in the white dwarf, which undergoes explosive burning and leads to the destabilization of the white dwarf. This explosion results in the complete disruption of the white dwarf and the ejection of its material into the interstellar medium. In contrast to core-collapse SN (SNcc), which are caused by the collapse of the nucleus of a massive star due to gravitational forces and can leave behind a neutron star or black hole, Type Ia SN are not associated with the death of a massive star. They are thought to produce elements like silicon, sulfur, and heavier elements like calcium, chromium, iron, and nickel, and are believed to be responsible for a significant fraction of these elements in the Universe. These elements are synthesized during the explosion, but do not remain in significant quantities after the supernova.

# 4

## THE XMM-NEWTON X-RAY TELESCOPE

---

X-ray telescopes, such as the Chandra Space Telescope, have been used for scientific research in the past and continue to be used today. The Chandra Telescope, launched by NASA in 1999, is known for its high image resolution and is particularly useful for studying galaxies, galaxy groups, and cluster galaxy structures.

European Space Agency (ESA) sent into space another telescope that is still in operation, XMM-Newton also known as X-Ray Multi-Mirror Mission, in 1999.

Its high spectral resolution allows for more accurate study of elemental abundances in various environments such as the ICM and IGrM. For this reason, XMM-Newton observations were chosen to study the temperature and elemental abundance distribution in the NGC 6284.



**Figure 4.1** Artist's portrayal of the XMM-Newton (ESA: *XMM-Newton Operations* n.d.)

## 4.1 Components of XMM-NEWTON

The XMM-Newton XRT weighs 4 tons and is 10 meters long. It holds the distinction of being the biggest scientific satellite ever launched by ESA and comprises 4 essential elements (Barré, Nye, Janin 1999).

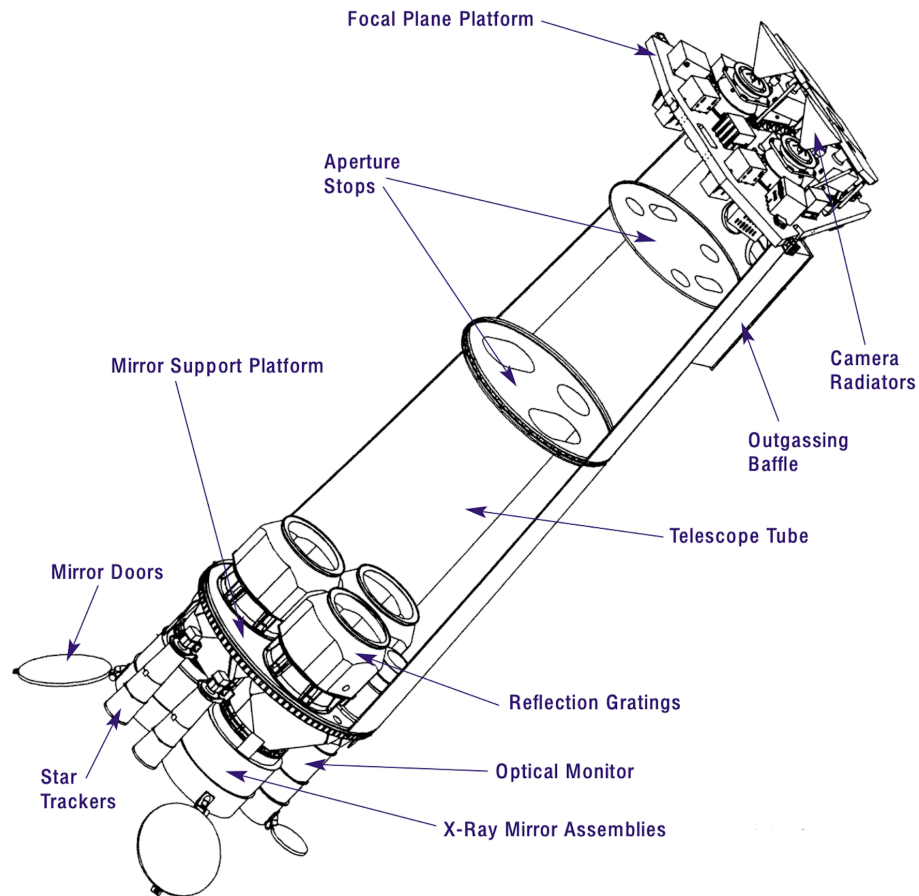


**Figure 4.2** The Physical Composition of XMM-Newton Telescope including X-Ray Mirror Assemblies and Focal Plane Cameras located at both ends of the Telescope Tube. (Barré, Nye, Janin 1999)

### 4.1.1 The Focal Plane Assembly

The focal plane instruments are located at the top of the satellite and are carried by the focal plane assembly (FPA). The focal plane instruments include 2 reflection gratings spectrometers (RGS), 2 European Photon Imaging Cameras (EPIC) MOS and 1 EPIC PN camera, data processing and power distribution units provide energy to the cameras.

### 4.1.2 Mirror Support Platform

The mirror support platform (MSP) platform houses two star trackers, three mirror assemblies and an optical monitor (OM). The mirror assembly consists of two RGS grating boxes, mirror modules and doors, entrance baffles and exit baffles.

### 4.1.3 Telescope Tube

The telescope tube (TT) with a length of 6.80m is located between FPA and MSP. It consists of a lower and an upper tube by virtue of its length. The upper section of the tube includes two doors that can be opened for venting and outgassing, known as reversible venting and outgassing doors (VOD), as well as a device for releasing gas, referred to as the outgassing buffer (OGB).

### 4.1.4 Service Module

The closed box of the service module (SVM) surrounds a central cone that holds the satellite subsystem. The SVM is connected to units that supply resources to the satellite. Two solar array wings, two S-band antennas and Telescope Sun Shield (TSS) are mounted on its arms.

## 4.2 The Orbit of XMM-Newton

In order to optimize the XMM-Newton satellite's goals in space, orbit selection considerations included ensuring that the orbital lifetime would be at least 10.25 years and maximizing scientific observation time, etc.

The orbit of XMM-Newton is an ellipse with a perigee and an apogee that the points on the orbit closest and farthest from the orbiting body. Apogee and perigee are 114 000 km and 7 000 km respectively. The orbital inclination, the angle between the orbital plane and the equator, is 40 degrees and the period, the time required to complete one orbit around the Earth, is 47.86 hours. Its orbit parameters are exhibited in table 4.1.

**Table 4.1** The XMM-Newton Orbit Parameters

Perigee	7000 km
Apogee	114 000 km
Inclination	40 deg
Period	47.86 h

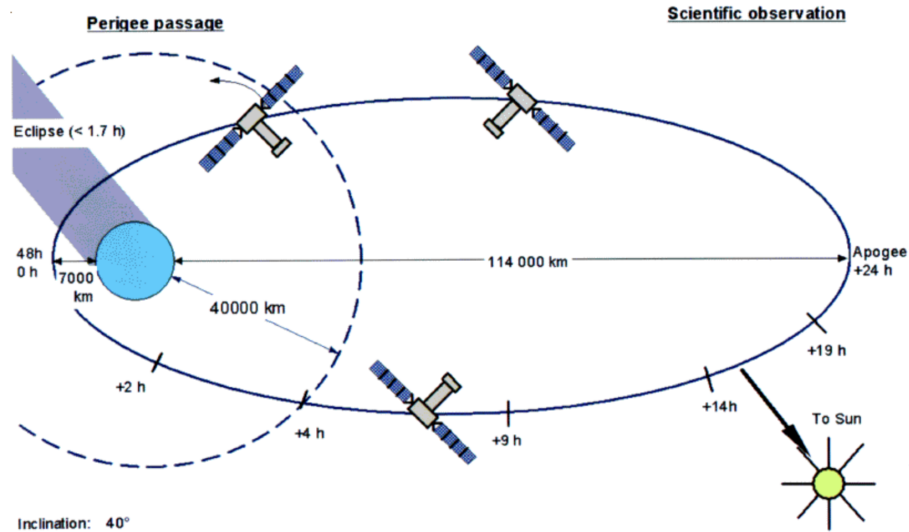


**Figure 4.3** The Schematic View of XMM-Newton Orbit (*HEASARC: XMM-Newton Mission Orbit n.d.*)

### 4.3 The Scientific Instruments of XMM-Newton

The XMM satellite is a very powerful X-ray space telescope whose main feature is three mirror modules that focus X-rays at a focal distance of 7.50 m onto five scientific cameras at the other end of the satellite. The XMM telescope has three scientific instruments: three EPIC cameras mounted at the focal points of the three mirror modules, two RGSs that record the spectrum produced by the two gratings, and one OM that provides optical/ultraviolet (UV) images (Bagnasco et al. 1999).

The XMM-OM, or the Optical/UV Monitor Telescope, is a separate device that is placed on the same platform as the X-ray mirror modules on XMM Newton. The X-ray field of view (FOV) is centered on a 17 arcmin<sup>2</sup> area, which encompasses a wavelength range between 170 nm and 650 nm. This allows for routine simultaneous observations of XMM targets in both the X-ray and ultraviolet/optical bands (Mason et al. 2001).

The RGS instrument uses reflection gratings to scatter X-rays collected and focused by the mirror module at different angles, similar to a prism. This creates a spectrum that can be picked up and studied using a charge coupled device (CCD) detector strip.

The RGS instrument is designed to provide high-precision measurements ( $E/\Delta E = 100$  to 500) in the soft X-ray range (6 to 38 Å or 2.1 to 0.3 keV) with a peak efficiency of 140 cm<sup>2</sup> at 15 Å (Den Herder et al. 2001). The unscattered X-rays are focused through the gratings to be captured by the EPIC cameras for imaging purposes.

The instrument EPIC consists of a camera unit, which includes a CCD detector unit, an analog electronic unit for camera control, an analog electronic unit for signal

conditioning, a digital signal processing unit, and a data set that handles general instrument control, connection to the observatory and processing unit and data formatting.

XMM-Newton observes and stores these data with each of the above scientific instruments. Its archive contains RGS, OM, and EPIC observational data of astronomical objects. We have used EPIC observational data for NGC 6284. The EPIC instrument is discussed in more detail in the next section.

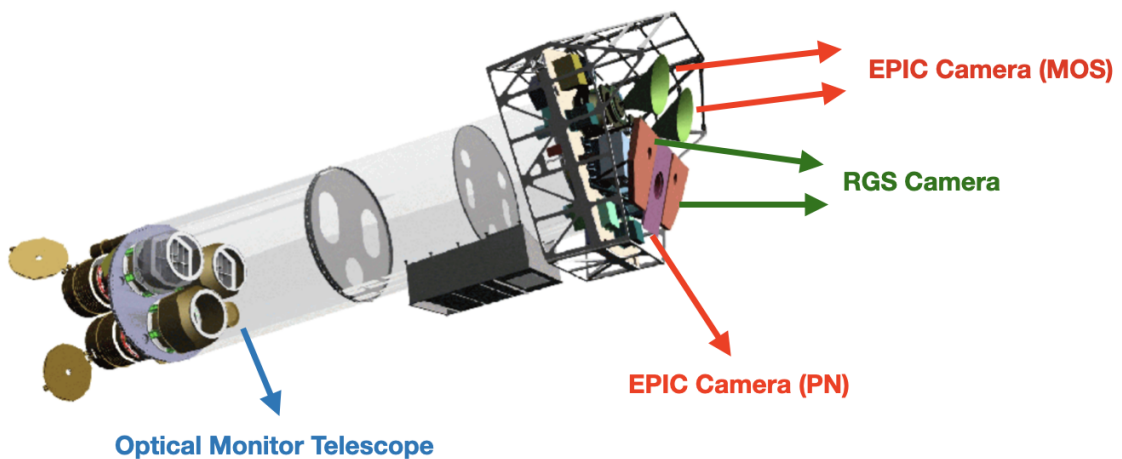


**Figure 4.4** The Scientific Instruments of XMM-Newton Orbit with 3 EPIC Camera (2 MOS and 1 PN), 2 RGS Camera and an Optical Monitor (*ESA: XMM-Newton Payload n.d.*)

#### 4.3.1 EPIC Instruments

The XMM-Newton spacecraft features an advanced imaging system, comprising of three X-ray cameras, one of which is the European Photon Imaging Camera (EPIC). This camera system comprises of two MOS (metal-oxide-semiconductor) CCD arrays, which are placed in the path of X-ray telescopes that are outfitted with reflection grating spectrometers (RGS). The EPIC instrument is placed at the focal point of the third X-ray telescope, which does not have any obstructions in its beam path. This instrument makes use of PN CCDs for detection and imaging. Both perform highly precise imaging observations on the field of view (FOV) of the telescope. They have a 30 arcmin FOV in the energy range of 0.15 keV to 15 keV.

When an incoming photon hits the semiconductor layer of the CCD, it generates an electron cloud, and the generated electrons are stored in pixels. MOS has seven front-illuminated CCDs in its cameras (Turner et al. 2001). On the focal point of the

optical axis is the central CCD. The two EPIC MOS cameras are rotated 90 degrees to each other. MOS cameras are positioned in the focal plane of the spacecraft so that the CCDs are orthogonal to each other.

The PN camera also has twelve back-illuminated PN CCDs with 3 x 1 cm. Four of the quadrants have 3 PN CCD subunits, each with 200 x 64 pixels, running in parallel (Strüder et al. 2001). CCDs can also indicate the exact time at which a particular X-ray photon hit them. The main difference between MOS and PN detectors is the time resolution. While MOS can distinguish between two X-ray photons falling on it 1.5 milliseconds apart, the PN detector has a much better time resolution of 0.03 milliseconds or 30 microseconds. MOS detectors, on the other hand, have a higher spatial resolution: they can distinguish objects that are about a quarter as large as those of a PN detector.

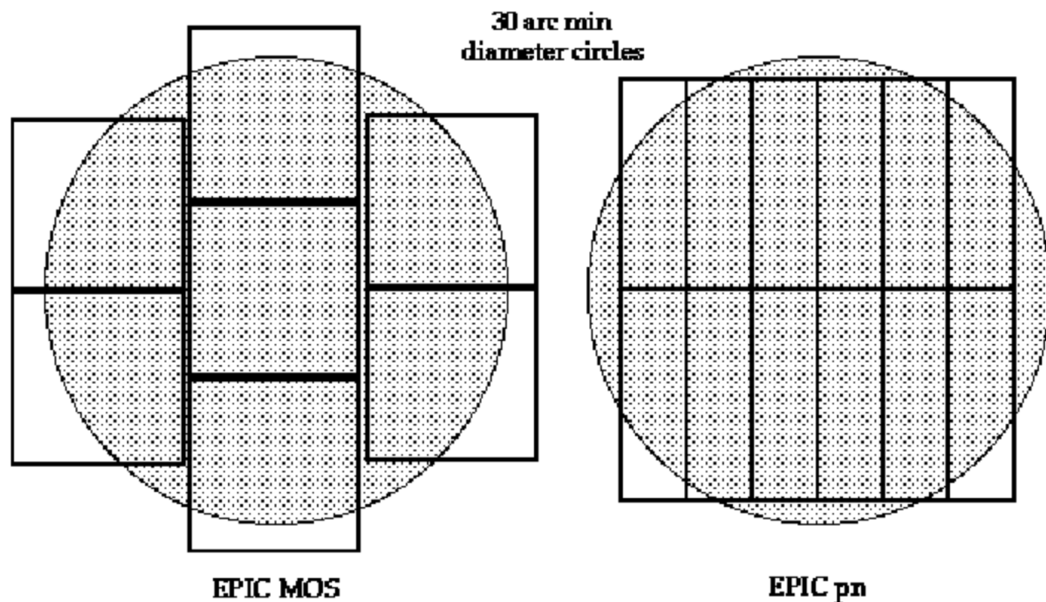


**Figure 4.5** The Sketch of EPIC MOS (left) and EPIC PN (right) CCDs arrays. The circle with shading represents a 30' diameter region. (ESA: EPIC CCDs n.d.)

## 5.1 Data Reduction

In this data analysis process, we followed ESAS Cookbook steps (Snowden, Kuntz 2014).

### 5.1.1 Observation

We analyzed observational data obtained with the XMM-Newton Space Telescope to profile the temperature and element abundance in the IGrM of the NGC 6482. For the GG, seven different observations were archived from 2006 to 2019 in the XMM-Newton Science Archive (*NXSA: XMM-Newton Science Archive* n.d.). We selected the observations with the longest duration and having the scientific product among the longest observation periods. The reason is that a longer observation period improves our statistics and leads to more accurate results. Detailed information about the observations can be found in the table 5.1.

**Table 5.1** Observation information of the NGC 6482 from the XMM-Newton data archive

Observation ID	RA	Dec	Duration	Exposure (s)
0822340301	17h 51m 48.80s	+23d 04' 19.0"	142700	3 EPIC, 18 OM, 2 RGS

### 5.1.2 Creating Cleaned Event Files

The data in observation data files (ODF) format given in the table were downloaded from the XSA. Data cleaning of the ODF files was performed using SAS version 10-9.1.0 and the latest calibration files.

The first step in the data cleaning process is to create a calibration index file (cif) with with the name **ccf.cif** from Current Calibration Files (CCF) file using the *cifbuild* task. Then, using the *odfingest* command, a new summary file with the extension *\*SUM.SAS* is created with the information from the data files and the calibration database (caldb).

In the next step, the *epchain* and *emchain* commands were used to create event files showing how many photons hit each pixel of the detector for MOS and PN cameras. Processed MOS and PN images with the *mos-filter* and *pn-filter* commands respectively.

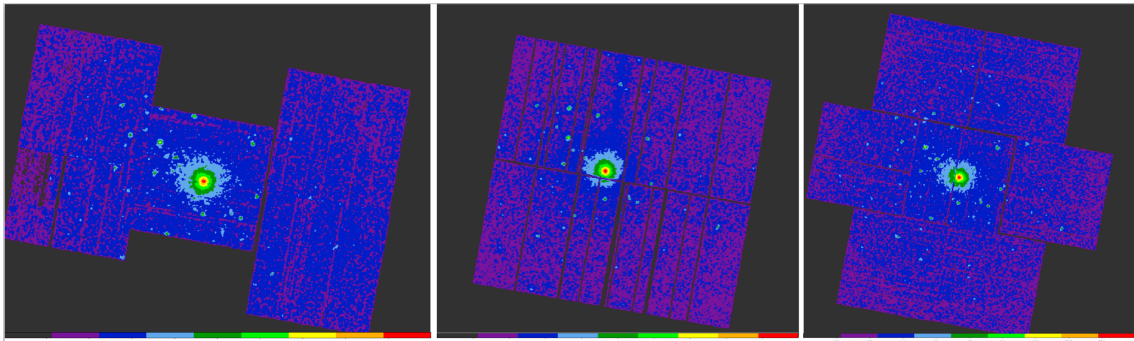


**Figure 5.1** MOS1 (left), MOS2 (middle) and PN (right) Images with created *mos-filter* and *pn-filter* task

Commands are utilized to eliminate soft proton (SP) contamination and create good time interval (GTI), with SPs (energies less than a few 100 keV) posing a threat to CCD detectors through non-ionizing dose leading to spectral resolution degradation. SP signals blend in with X-ray photons, resulting in an extended background component. After this step, we now have our first images, light curves (lc) and GTI files for all EPIC cameras.

In the Figure 5.1 can be seen easily that CCD 6 and CCD 3 were excluded for MOS1. The reason is that a micrometeorite hit CCD 6 on 2005 and a micrometeorite hit CCD 3 on 2012. Scientific observations are continuing normally with MOS1, but now without data from CCD3 and CCD6 as well. The event has also increased the noise level in CCD4.

The light curves of EPIC cameras are presented in the Figure 5.2. The energy range of MOS-1 and MOS-2 CCDs is 0.2-10 keV and the energy range of PN CCD is 0.5-10 keV. The average photon count rate from the MOS1 is about 0.9 counts/rate, MOS2 is about 0.9 and that from the PN detector is about 4 counts/s. Count deviations above these average values come from sources outside the GG. Since the PN detector is more sensitive in the hard energy range, the number of photons received is higher in the hard energy range.

Finally, the GTI files used to find the cleaned exposures which displayed in table 5.2 for all EPIC cameras.

Using the *mos-spectra* and *pn-spectra* commands, new event files of all FOV covering the energy range 0.4 - 7.2 keV were generated from the event files obtained from the *mos-filter* task and *pn-filter* task.

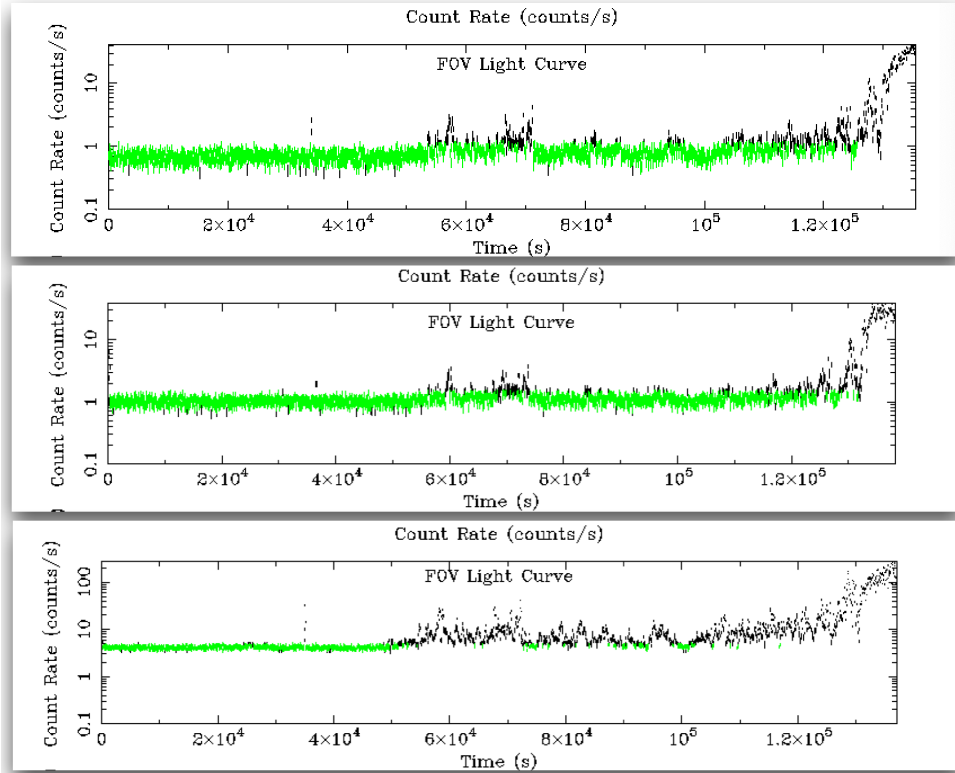


**Figure 5.2** Light Curves of MOS1 (top), MOS2 (middle) and PN (bottom)

**Table 5.2** EPIC Cameras and Their Cleaned Exposures

EPIC Camera	Cleaned Exposure (ks)
MOS 1	~ 105.72
MOS 2	~ 112.62
PN	~576.60

Quiescent Particle Background (QPB) is the background noise created by high-energy particle interactions with detectors and their surrounding materials (Kuntz, Snowden 2008). Spectra and images of the QPB produced separately for each of the three cameras using the *mos-back* and *pn-back* procedure.

By combining the images created from EPIC cameras with the task *comb*, combined image containing point sources was produced with the parameter *mask=0*.

### 5.1.3 Point Source Detection

In general, *cheese* task is used to detect point sources but we used Chandra's *wavdetect* task to find the point sources coordinates. That is why Chandra's image resolution is higher than that of the XMM-Newton telescope; it is better able to detect point sources in the IGrM. We made sure that the radius of point sources must be at least

0.6" because of the lower image resolution of XMM-Newton.

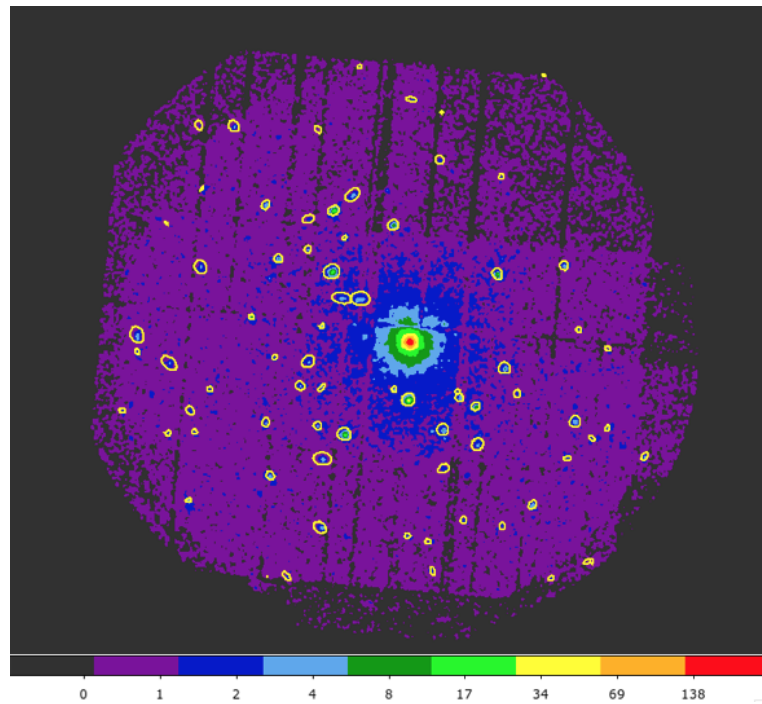


**Figure 5.3** EPIC (MOS and PN) combined image: yellow circles are symbolized detected regions of point sources with Chandra *wavdetect* task

We converted the coordinates of the detected point sources into the coordinate format that Xmm-Newton can use and we obtained the cheese images with the *make\_mask* command.

Images created from EPIC cameras were combined with the task *comb*, the point source was cleaned with the parameter *mask=1* and the image without points sources was created.

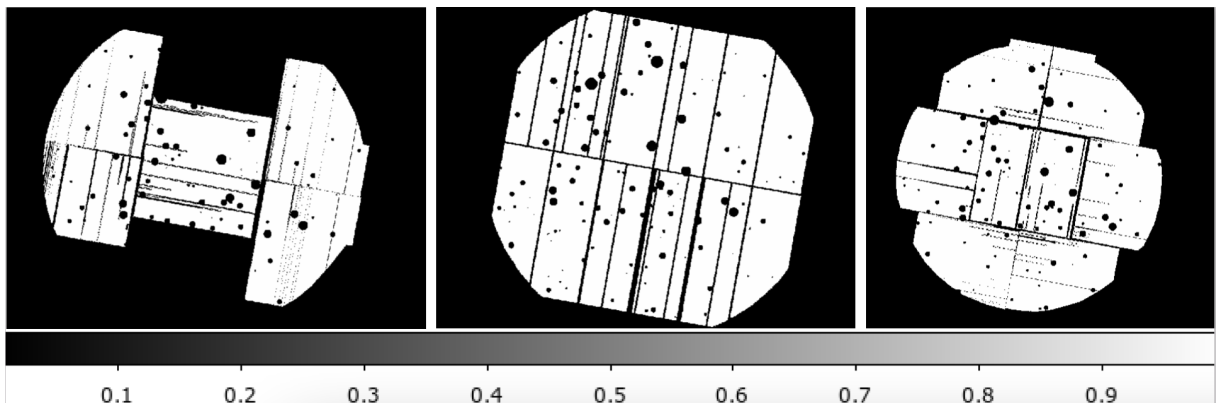


**Figure 5.4** MOS1 (left), MOS2 (middle) and PN (right) cheese images created with *make\_mask*

#### 5.1.4 Creating Spectrum Files

By reusing the *mos-spectra*, *mos-back*, *pn-spectra* and *pn-back* commands, we create new concentric regions (0–20", 20–50", 50–90", 90–140") presented in the Figure 5.5. The black circle symbolizes the 0–20", the red circle signifies the 20–50", the green circle indicates the 50–90", and finally, the cyan circle represents the 90–140". After 140" region, we could not measure the parameters consistently.

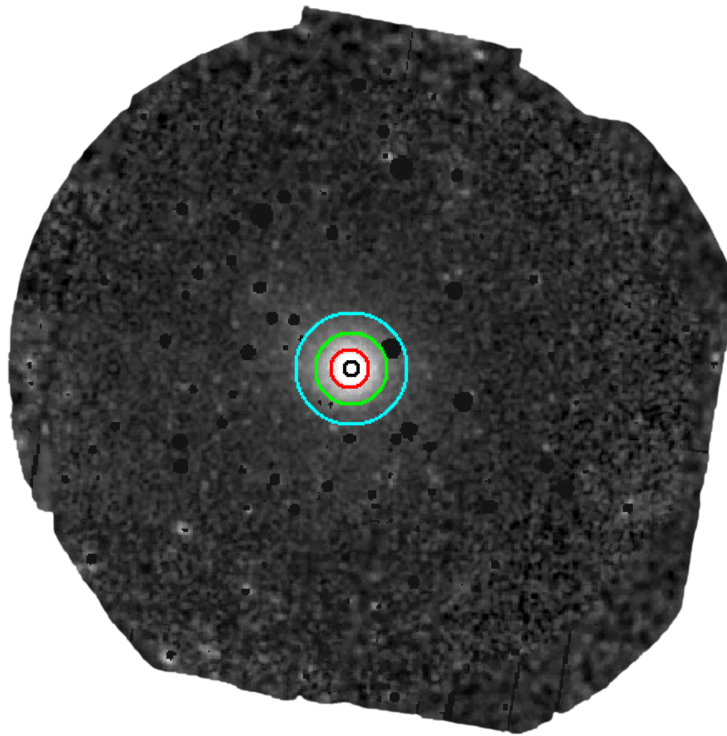


**Figure 5.5** EPIC combined and cleaned point sources image of NGC 6482

Determined the center of NGC 6284 in detector coordinates using the *xmmselect* task and acquired Ancillary Response File (ARF) and Response Matrix Files (RMF) for selected regions for each EPIC camera.

## 5.2 BACKGROUND ANALYSIS

Effective background modeling is key to obtaining accurate results from source radiation. To achieve this, all components, such as cosmic X-ray background (CXB) and noncosmic X-ray background (NXB), should be modeled optimally (Snowden, Mushotzky, et al. 2008).

### 5.2.1 Noncosmic X-Ray Background

The XMM-Newton Charge Coupled Devices (CCDs) are intended to detect X-rays with energies between 0.15 and 15.0 keV. As a result, the CCDs will record not only the X-ray

signals emitted by the object being observed, but also any photons within the 0.15 - 15.0 keV energy range that happen to be present. This additional contamination is called the Noncosmic X-ray Background (NXB). The NXB is made up of two significant components: Solar Wind Charge Exchange and Instrumental Lines.

### 5.2.1.1 Solar Wind Charge Exchange

The Solar Wind Charge Exchange (SWCX) refers to the interaction between ions in the solar wind and neutral atoms. The solar wind is a flow of charged particles released by the Sun. When a solar wind ion approaches a neutral atom, it can transfer some of its charge to the atom via collision. This charge transfer can cause the neutral atom to ionize or gain charge. The SWCX has various impacts on the Earth's upper atmosphere and satellite operations and other activities in near-Earth space.

The SWCX produces X-rays that are not related to the astronomical objects being studied and can cause contamination in X-ray observations. To remove contamination from observations, the SWCX lines must be modeled. The most prominent SWCX lines detectable by XMM-Newton are the O VII and O VIII lines, which have energies of  $\sim 0.56$  keV and  $\sim 0.65$  keV respectively. Our analysis involved Gauss components to mitigate this effect.

$$S_{swcx} = gauss + gauss \quad (5.1)$$

The center lines of the Gauss functions are fixed at energies of 0.56 keV and 0.65 keV, respectively. The widths of the Gauss functions are set to 0.0 and their normalizations are set free."

### 5.2.1.2 Instrumental Lines

The materials used in the construction of XMM-Newton interact with the X-rays collected, producing additional X-rays. These rays, which are not from the observed object, cause contamination in the data and are known as instrumental lines. It is necessary to model these instrumental lines.

$$S = gauss + gauss \quad (5.2)$$

There are several known instrumental lines that can be detected by XMM-Newton, each with a specific energy or wavelength. These lines include Al  $K\alpha$  ( $\sim 1.49$ ), Si  $K\alpha$  ( $\sim 1.75$  keV) for MOS1 and MOS2, and low energy Si  $K\alpha$  ( $\sim 1.75$  keV) for PN. We modeled these lines but Lines of elevated energy are also produced by elements

including Au, Cr, Mn, Fe, Ni, and Zn (Snowden, Collier, Kuntz 2004). To model Al  $K\alpha$  and Si  $K\alpha$  lines, we added Gauss components by setting their widths to 0.0 and normalizations free.

## 5.2.2 Kozmik X-ray Background

The Cosmic X-ray Background (CXB) is a contaminant that primarily comprises diffuse emission at energies lower than around 1 keV, having a thermal spectrum marked by prominent emission lines (Fabian, Barcons 1992). The Local Hot Bubble (LHB), the Galactic Halo (GH), and Unresolved Point Sources (UPS) are three key elements of CXB.

### 5.2.2.1 Local Hot Bubble

The LHB is a plasma region that encompasses and considered close to the Sun (so it is named "local") characterized by a temperature of roughly 0.1 keV and low density.

An unabsorbed thermal model expresses the emission coming from the LHB because The Galactic interstellar medium's (ISM) hydrogen column density is not absorbe the LHB emission.

$$S_{lhb} = apec \quad (5.3)$$

with a temperature of 0.1 keV initial parameter. The abundance parameter of the model is set at 1.0  $Z_{\odot}$  and the redshift is fixed at 0.0 therefore LHB originates from the galaxy.



**Figure 5.6** The image illustration of the local hot bubble (NASA, *Local Hot Bubble* n.d.)

### 5.2.2.2 Galactic Halo

Inside the LHB, there is the Milky Way and its galactic halo (GH). The GH surrounds the Milky Way, while the LHB surrounds a portion of the Orion Arm. The GH is divided into two components: hot and cold. These components have initial energies of approximately 0.25 keV and 0.1 keV respectively.

$$S = phabs * apec \quad (5.4)$$

The abundance parameter of the apec is set at 1.0  $Z_{\odot}$  and the redshift is fixed at 0.0. The parameters are set this way because the GH components also originates from the galaxy.

### 5.2.2.3 Unresolved Point Sources

Unresolved point sources (UPS) is the third major component of the CXB. An absorbed power law represents UPS and its  $\Gamma$  is set to 1.45 keV.

$$S_{ups} = phabs * powerlaw \quad (5.5)$$

### 5.2.3 Background Modelling

With NASA's HEASARC X-Ray tools, the hydrogen column density ( $N_H$ ) and average background count rate of NGC 6482 in X-Rays were determined using data from the ROSAT All Sky Survey (RASS) (*HEASARC X-ray Background Tool* n.d.). As a result, the downloaded files from the tool were fitted using the XSPEC TCL script and the parameters obtained from the fit are used to background modelling (*XSPEC TCL Scripting Documentation* n.d.).

Then, we selected an annuli(400" – 500") as far from the galaxy center as possible for background modelling. Extracted annuli was modeled using the parameters from the rass fit and new parameters were obtained for CXB.

Finally, our total model was as follows for background.

$$S_{BACKGROUND} = gaussian_{IL:1.49} + gaussian_{IL:1.75} + constant * constant (gaussian_{SWCX:0.56} + gaussian_{SWCX:1.49} + apec_{LHB} + (apec_{GH} + powerlaw_{UPS})phabs$$

Additionally we add separate *bknpow* (broken power law) model for the residual SP contamination and the  $E_{break}$  (the break point) for the energy was set to 3.0 keV.

### 5.3 Source Analysis

Prior to analyzing the x-ray emission mechanisms, we utilized the `apec` and `vgadem` codes, which can take into consideration the bremsstrahlung, two photon emission, and radiative recombination processes originating from the NGC 6482 GG.

#### 5.3.1 Astrophysical Plasma Emission Code

The APEC code covers parameters of temperature, metallicity, normalization, and redshift (Smith et al. 2001). Temperature is calculated in keV and metallicity in solar units. The redshift parameter is entered as the redshift value of the source being analyzed. For NGC 6482, the redshift value is 0.012, so we fixed this parameter to this value. Normalization is calculated using the following formula.

$$Norm = \frac{10^{-14}}{4\pi[D_A(1+z)]^2} \int n_e n_H dV \quad (5.6)$$

In this formula,  $D_A$  is the angular diameter to the source in cm,  $n_e$  is the electron density,  $n_H$  is the hydrogen density, and  $dV$  is the volume element. `Apec` performs all these calculations using the atomic database (ATOMDB) (Foster et al. 2012).

#### 5.3.2 Multi-temperature with Gaussian Distribution of Emission Measure

The GADEM code models plasma emission through a Gaussian distribution with multiple temperatures, similar to the APEC or MEKAL models. It has parameters for mean and sigma temperature and a switch parameter that determines whether to use the MEKAL or APEC code. In the analysis, the switch parameter was set to 2 to use the APEC code. The VGADEM model calculates metal abundance for a greater number of elements than the GADEM model. We used VGADEM for measuring more elements.

### 6.1 Temperature and Metal Distributions

We talked about how we modeled the source and background emissions in the previous section. Additionally, we add power law model to the source components for low mass X-ray Binary (LMXB). Finally, our total model with background and source component is

$$S_{TOTAL} = \text{gaussian}_{IL:1.49} + \text{gaussian}_{IL:1.75} + \text{constant} * \text{constant} (\text{gaussian}_{SWCX:0.56} + \text{gaussian}_{SWCX:1.49} + \text{apec}_{LHB} + (\text{apec}_{GH} + \text{powerlaw}_{UPS})\text{phabs} + (\text{vgadem}_{source} + \text{powerlaw}_{LMXB})\text{phabs})$$

where the first *constant* is the solid angle of EPIC detectors and the second *constant* is scaling factor for the difference between effective areas of MOS1, MOS2 and PN.

By using these models, the spectra of four regions with equal centers were obtained using XSPEC (K. Arnaud, Dorman, Gordon 1999). The parameters of temperature, Mg, Fe, S and Si were obtained from the extracted spectra for each region. The ASPL abundance table and cstat was used as the metal abundance table and the statistic, with  $N_H$  set to 0.082 (Asplund et al. 2009) , (Cash 1979).

We are presenting above spectrum of each region in the Figures 6.1, 6.2, 6.3, 6.4. The temperature and its sigma value, normalization and statistics with d.o.f. (degrees of freedom) are listed in the Tables 6.1, 6.2, 6.3, 6.4. The indicated temperature shows that a substantial part of the plasma has that value, while the sigma range indicates the temperature range where the rest of the plasma is located.

Finally, we compared our results from temperature and metal distributions with the literature works which demonstrated in the Figures 6.5 and 6.6.

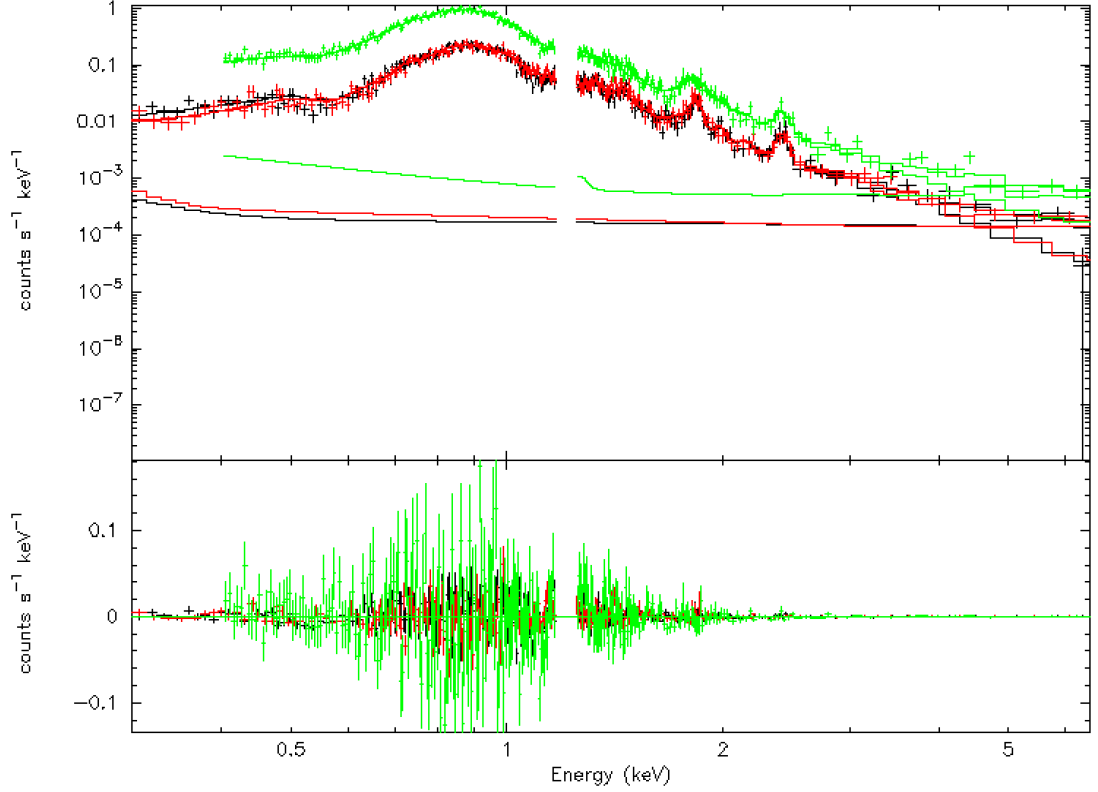


**Figure 6.1** EPIC spectra of 0-20 arcsec region of NGC 6482

In some regions of the NGC 6482 GG spectrums, we encountered excessive emission in the 1.17-1.25 keV energy range, whose origin could not be determined. We ignored this energy range because removing the emission from the spectrum did not change the measured element values. Therefore in 0–20'' we ignored the energy range. Our results for this region are presented in the Table 6.1.

**Table 6.1** Best fit *vgadem* model parameters with  $1\sigma$  errors for 0-20 arcsec region of NGC 6482

Region (arcsec)	kT (keV)	kT $\sigma$ (keV)	Normalization ( $\times 10^{-3}$ )	cstat/d.o.f.
0-20	$0.8263^{+0.003}_{-0.003}$	0.139	$1.196^{+0.0048}_{-0.079}$	3211/3639

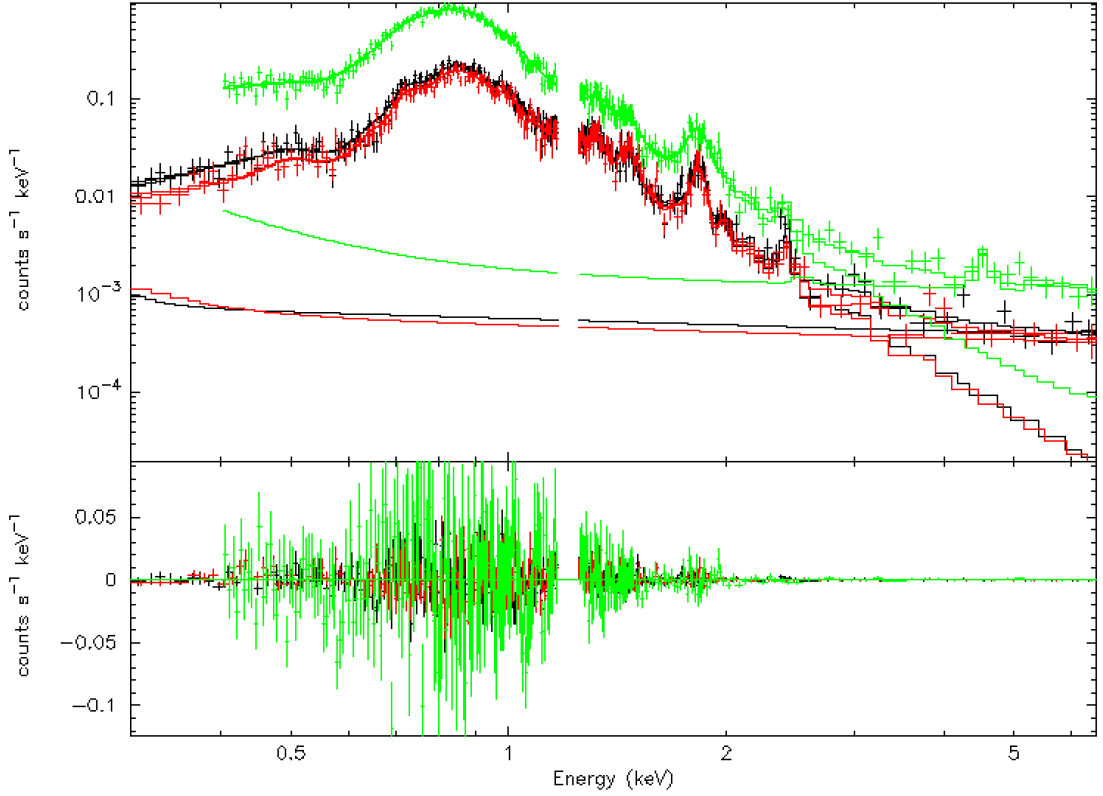


**Figure 6.2** EPIC spectra of 20-50 arcsec region of NGC 6482

As we did in the previous region, in this area we also encountered excessive emission of unknown origin, so we eliminated the 1.17-1.25 keV energy range just as before and the results for the region of 20 – 50” are given in the Table 6.2.

**Table 6.2** Best fit *vgadem* model parameters with  $1\sigma$  errors for 20-50 arcsec region of NGC 6482

Region (arcsec)	kT (keV)	kT $\sigma$ (keV)	Normalization ( $\times 10^{-3}$ )	cstat/d.o.f.
20-50	$0.756^{+0.003}_{-0.003}$	0.149	$15.3^{+0.007}_{-0.011}$	3323/3638

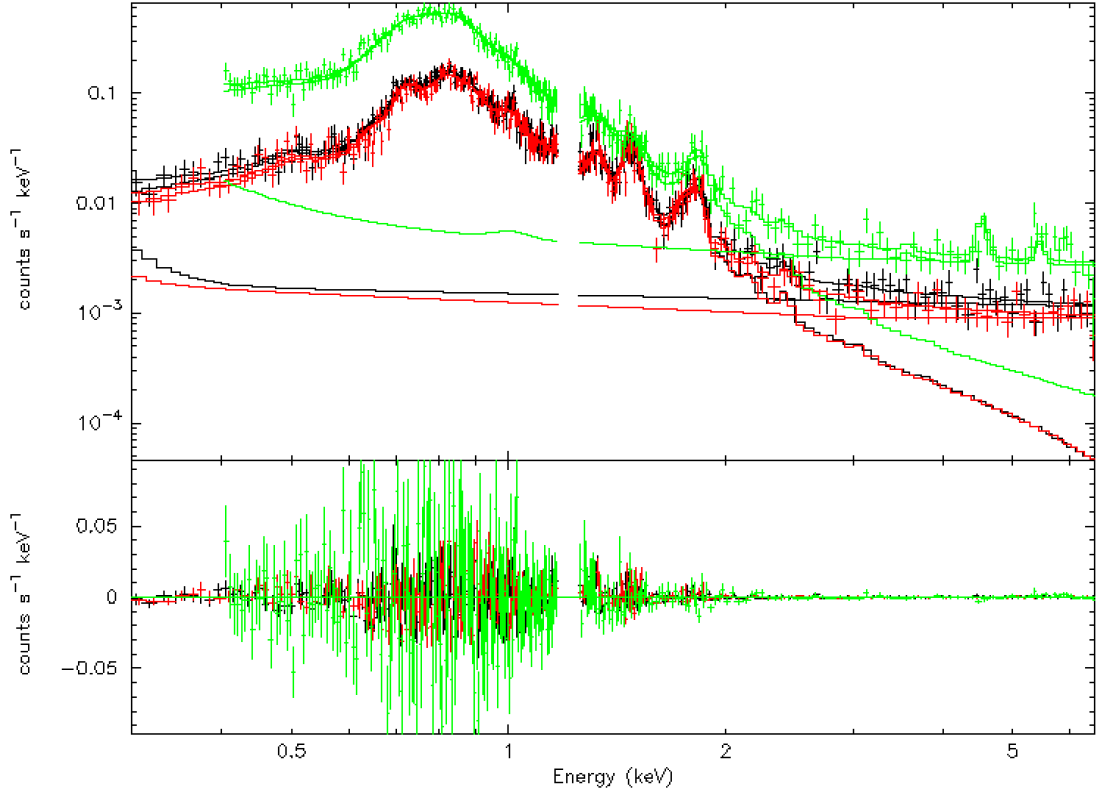


**Figure 6.3** EPIC spectra of 50-90 arcsec region of NGC 6482

In this region as well, we encountered extra emission of unknown origin and removed it from the spectrum and the Table 6.3 exhibits the results of 50 – 90” region.

**Table 6.3** Best fit *vghadm* model parameters with  $1\sigma$  errors for 50-90 arcsec region of NGC 6482

Region (arcsec)	kT (keV)	kT $\sigma$ (keV)	Normalization ( $\times 10^{-3}$ )	cstat/d.o.f.
50-90	$0.628^{+0.006}_{-0.011}$	0.207	$0.059^{+0.006}_{-0.003}$	3957/3642

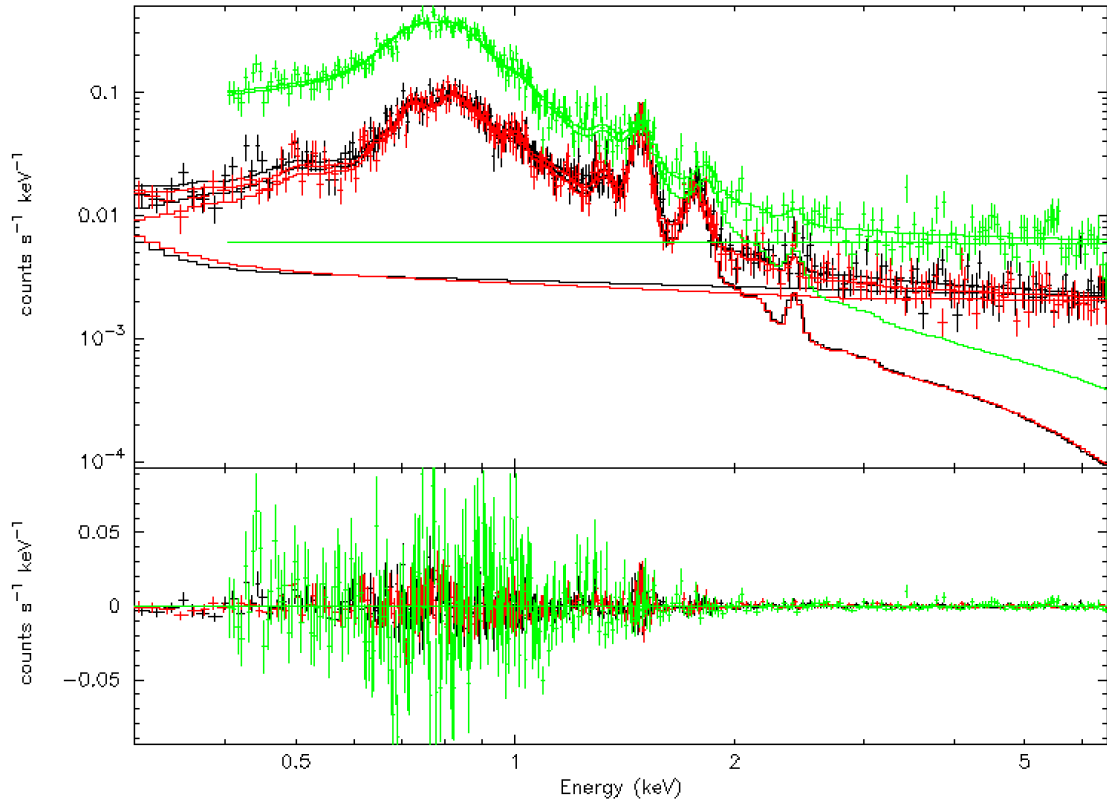


**Figure 6.4** EPIC spectra of 90-140 arcsec region of NGC 6482

Since we did not encounter extra emission in the last region, there was no need to remove the 1.17-1.25 keV energy range from the spectrum and the Table 6.4 shows the results for 90 – 140'' region.

Finally, the results for the distributions of Fe, Mg, Si and S elements for all region are presented in the Table 6.5.

**Table 6.4** Best fit *vgradem* model parameters with  $1\sigma$  errors for 20-50 arcsec region of NGC 6482

Region (arcsec)	kT (keV)	kT $\sigma$ (keV)	Normalization ( $\times 10^{-3}$ )	cstat/d.o.f.
90-140	$0.563^{+0.011}_{-0.014}$	0.227	$0.032^{+0.003}_{-0.002}$	4132/3692

**Table 6.5** Best fit *vgadem* model parameters of abundance with  $1\sigma$  errors for all four annuli

Region (arcsec)	Fe $Z_{\odot}$	Mg $Z_{\odot}$	Si $Z_{\odot}$	S $Z_{\odot}$
0-20	$0.866^{+0.003}_{-0.003}$	$0.995^{+0.115}_{-0.067}$	$0.773^{+0.088}_{-0.052}$	$1.378^{+0.201}_{-0.013}$
20-50	$0.929^{+0.080}_{-0.043}$	$1.146^{+0.050}_{-0.081}$	$1.101^{+0.134}_{-0.077}$	$1.135^{+0.248}_{-0.017}$
50-90	$0.639^{+0.103}_{-0.044}$	$0.696^{+0.154}_{-0.074}$	$0.799^{+0.171}_{-0.086}$	$0.599^{+0.327}_{-0.222}$
90-140	$0.5398^{+0.026}_{-0.041}$	$0.419^{+0.098}_{-0.072}$	$0.470^{+0.108}_{-0.084}$	$1.299^{+0.454}_{-0.365}$

## 6.2 Discussion

We conducted a thorough examination of the XMM-Newton data with ID 0822340301 for NGC 6482, a group that is known as a fossil group. Our analysis was based solely on the data obtained from the EPIC detectors. We present the results of our analysis which pertain to the distribution of temperature and elements including Fe, S, Si and Mg within the IGrM.

Fossil groups, due to their lack of major galaxy mergers or cluster formations, are considered a relaxed structure. As a result, they are ideal environments for the formation of cool cores and are comparable to cool-core clusters (Aguerri et al. 2011). In the  $0-0.1r_{200}$  region of this particular fossil group, the cooling time is shorter than the Hubble Time (Khosroshahi, Laurence R Jones, Ponman 2004). It was anticipated that the temperature would drop towards the center, however, our findings indicate the opposite. In the Figure 6.5, the temperature of the IGrM actually increases towards the center, consistent with the conclusions reached by (Buote 2017).

As shown in the Figure 6.6, we obtain the abundance profiles of Fe, Mg, Si, and S to the extent of  $0.16r_{500}$  and compared with average GG and GC samples in the CHEERs paper (François Mernier, Plaa, et al. 2017).

In the central  $0-0.02r_{500}$  region, Fe and Si exhibit complete concordance, while Mg and S displays an amount  $\sim 2$  and  $\sim 1.5$  times higher than the average amount in GG and GC. In the second  $0.02-0.06r_{500}$  region, although not significantly, Fe and S exhibit an uptick relative to GG and GC but its uncertainty is also high. In the third  $0.06-0.10r_{500}$  region, S and Fe displayed concordance with GG and GC, but Mg and Si revealed a noticeable rise. In the last  $0.06-0.10r_{500}$  region, S and Fe displayed concordance with

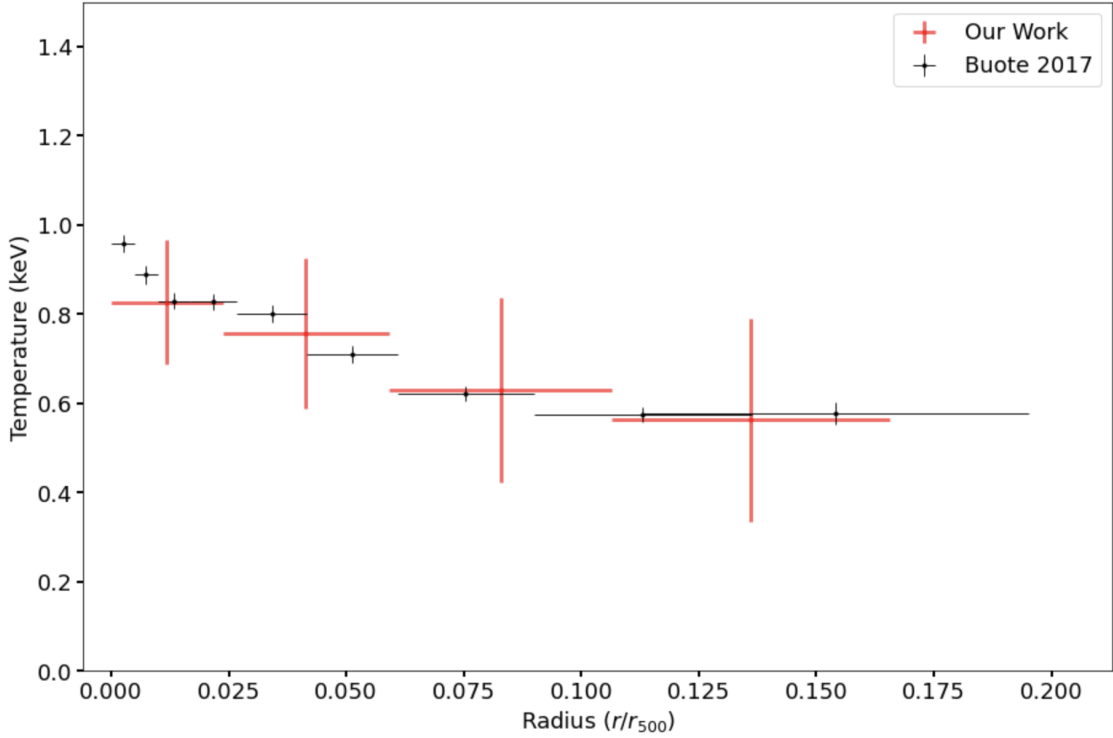


**Figure 6.5** The derived radial temperature profile is shown. The indicated temperature here demonstrates the mean temperature of the plasma and the red vertical lines presents the sigma temperature.

GG and GC, but Mg and Si revealed a noticeable rise.

All elements, with the exception of S, are compatible with GG and GC in the  $0.1-0.16r_{500}$  region. However, this value is probably a spectral artifact. Because when there is a clear increase in one element, we expect to see a similar increase in other elements produced by the same nucleosynthesis mechanisms. For example, despite being synthesized by the same mechanisms, Si does not show an increase consistent with this situation.

The reason of the unexpected increase could be related to low temperature. The temperature in the  $0.1-0.16r_{500}$  region was measured to be  $0.563^{+0.011}_{-0.014}$  keV. The line emission of S is below the background emission at these temperatures, making it difficult to measure accurately. Therefore, we discarded this S measurement.

Overall,

- i) Fe demonstrates compatibility with GG and GC profiles across all regions.
- ii) We observed that noncompatible abundance values of measured elements are always higher than the GG and GC average.
- iii) As the radius increase, element abundances converge towards a common value with GG and GC average.

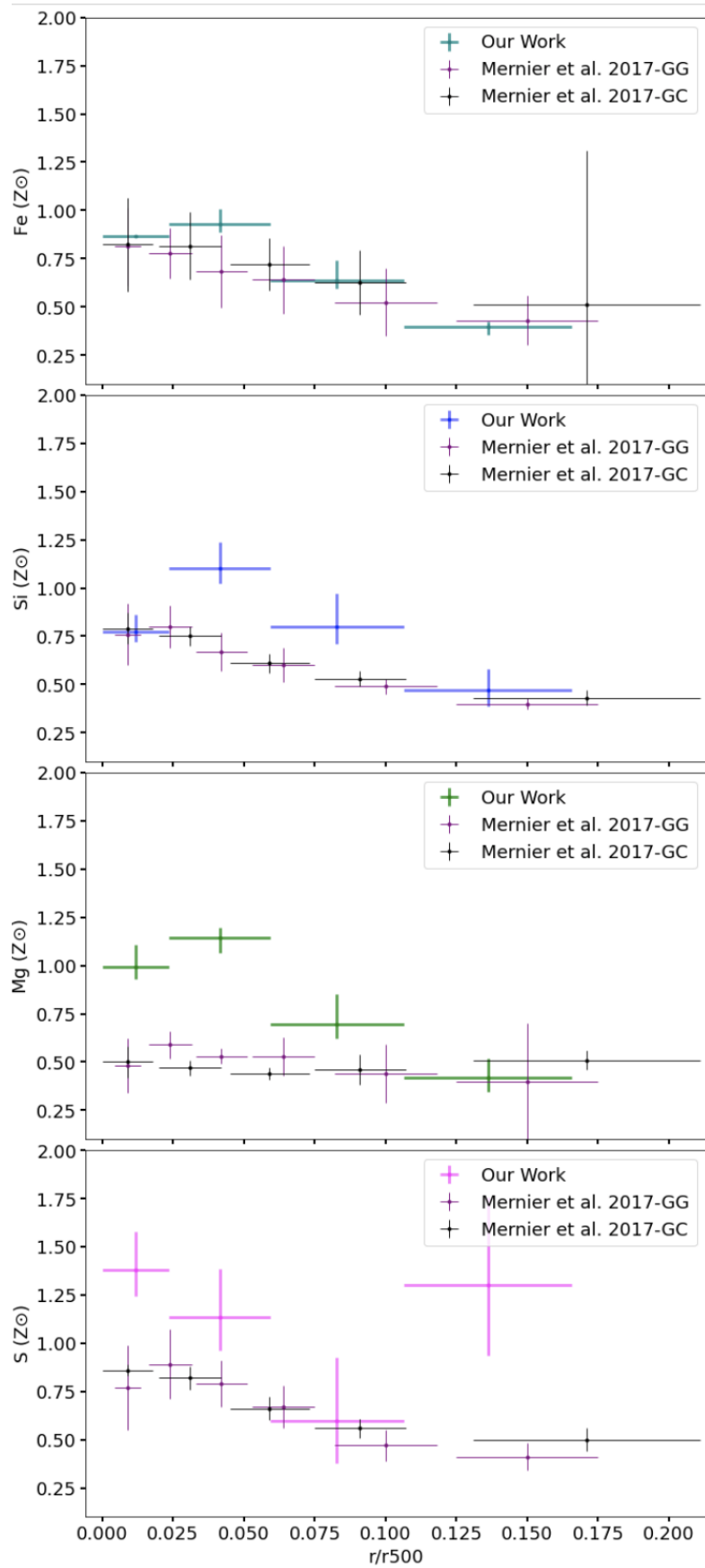


**Figure 6.6** The derived and compared radial Fe, Si, Mg and S profile is shown.

The possible causes for the observed variations in the central region of the fossil group, NGC 6482, could be attributed to two factors. Firstly, the activity happening within the central bright giant elliptical galaxy of the fossil group may be influencing the central and adjacent areas. The convergence of all the values we measured in the outermost region supports this hypothesis. However, to gain a more comprehensive understanding, further investigations need to be conducted in the outskirts of the group.

Secondly, the differences near the center of the group could be a characteristic behavior of the fossil groups that suppress SNcc products or enhance SNIa products. We observed that elements that show an increase according to the average GG and GC profiles in our profiles imply a relatively higher contribution of SNcc. The maximum relative increase was observed in Mg ( $\sim 2.0$ ), which is the main product of SNcc, while no relative increase was observed in Fe, which is largely produced by SNIa. The common products, S and Si, showed no increase in one (with high error margin), and lower level increase ( $\sim 1.5$ ) in the other.

It is important to note that our examination was limited to a single object, so it is not possible to conclude whether the chemical enrichment behavior observed in this study is a widespread trend in fossil groups or unique to this particular group. Further extensive studies may provide additional insights into the origin of this behavior.

## REFERENCES

---

- Aguerri, JAL et al. (2011). “Fossil groups origins-I. RX J105453. 3+ 552102 a very massive and relaxed system at  $z \sim 0.5$ ”. In: *Astronomy & Astrophysics* 527, A143.
- ALADIN: *Astronomical Atlas and Data Image Server* (n.d.). <https://aladin.u-strasbg.fr>. [Online]; Available: [Accessed: 05-Feb-2023].
- Andrew Howell, D et al. (2006). “The type Ia supernova SNLS-03D3bb from a super-Chandrasekhar-mass white dwarf star”. In: *Nature* 443.7109, pp. 308–311.
- Arnaud, Keith, Ben Dorman, Craig Gordon (1999). “XSPEC: An X-ray spectral fitting package”. In: *Astrophysics Source Code Library*, ascl-9910.
- Asplund, Martin et al. (2009). “The chemical composition of the Sun”. In: *Annual review of astronomy and astrophysics* 47, pp. 481–522.
- Bagnasco, G et al. (1999). “The scientific instruments on-board XMM- Technical highlights”. In: *ESA bulletin* 100, pp. 21–29.
- Barré, H, H Nye, G Janin (1999). “An overview of the XMM observatory system”. In: *ESA Bulletin* 100, pp. 15–20.
- Biviano, Andrea (2000). “From Messier to Abell: 200 years of science with galaxy clusters”. In: *arXiv preprint astro-ph/0010409*.
- Böhringer, Hans (2014). “X-ray observations of the chemical abundances in the Intra-Cluster Medium”. In: *arXiv preprint arXiv:1403.5261*.
- Böhringer, Hans, Norbert Werner (2010). “X-ray spectroscopy of galaxy clusters: studying astrophysical processes in the largest celestial laboratories”. In: *The Astronomy and Astrophysics Review* 18.1, pp. 127–196.
- Buote, David A (2017). “The Unusually High Halo Concentration of the Fossil Group NGC 6482: Evidence for Weak Adiabatic Contraction”. In: *The Astrophysical Journal* 834.2, p. 164.
- Cash, Webster (1979). “Parameter estimation in astronomy through application of the likelihood ratio”. In: *The Astrophysical Journal* 228, pp. 939–947.
- Clayton, Donald D (1983). *Principles of stellar evolution and nucleosynthesis*. University of Chicago press.
- COSMOS - *The SAO Encyclopedia of Astronomy: Supernova Classification* (n.d.). <https://astronomy.swin.edu.au/cosmos/S/supernova+classification>. [Online]; Available: [Accessed: 05-Feb-2023].
- Den Herder, JW et al. (2001). “The reflection grating spectrometer on board XMM-Newton”. In: *Astronomy & Astrophysics* 365.1, pp. L7–L17.
- Dupke, Renato A et al. (2022). “Independent Evidence for earlier formation epochs of fossil groups of galaxies through the intracluster light: the case for RX J100742. 53+ 380046.6”. In: *The Astrophysical Journal* 936.1, p. 59.
- Eigenthaler, Paul, Werner W Zeilinger (2007). “The Search for Fossil Groups of Galaxies”. In: *Astronomische Nachrichten* 328.7, p. 699.

- ESA: EPIC CCDs (n.d.). [https://xmm-tools.cosmos.esa.int/external/xmm\\_user\\_support/documentation/uhb/epic.html](https://xmm-tools.cosmos.esa.int/external/xmm_user_support/documentation/uhb/epic.html). [Online]; Available: [Accessed: 05-Feb-2023].
- ESA: XMM-Newton Operations (n.d.). [https://www.esa.int/Enabling\\_Support/Operations/XMM-Newton\\_operations](https://www.esa.int/Enabling_Support/Operations/XMM-Newton_operations). [Online]; Available: [Accessed: 05-Feb-2023].
- ESA: XMM-Newton Payload (n.d.). <https://www.cosmos.esa.int/web/xmm-newton/xmm-pay1>. [Online]; Available: [Accessed: 05-Feb-2023].
- Fabian, AC, X Barcons (1992). “The origin of the X-ray background”. In: *Annual review of astronomy and astrophysics* 30.1, pp. 429–456.
- Foster, AR et al. (2012). “Updated atomic data and calculations for X-ray spectroscopy”. In: *The Astrophysical Journal* 756.2, p. 128.
- Gamow, George (1946). “Expanding universe and the origin of elements”. In: *Physical review* 70.7-8, p. 572.
- HEASARC X-ray Background Tool (n.d.). <https://heasarc.gsfc.nasa.gov/cgi-bin/Tools/xraybg/xraybg.pl>. [Online]; Available: [Accessed: 05-Feb-2023].
- HEASARC: XMM-Newton Mission Orbit (n.d.). [https://heasarc.gsfc.nasa.gov/docs/xmm/about\\_satellite.html](https://heasarc.gsfc.nasa.gov/docs/xmm/about_satellite.html). [Online]; Available: [Accessed: 05-Feb-2023].
- Hickson, Paul (1982). “Systematic properties of compact groups of galaxies”. In: *The Astrophysical Journal* 255, pp. 382–391.
- (1997). “Compact groups of galaxies”. In: *Annual review of Astronomy and Astrophysics* 35.1, pp. 357–388.
- HyperLeda: Database for physics of galaxies (n.d.). <http://leda.univ-lyon1.fr>. [Online]; Available: [Accessed: 05-Feb-2023].
- Jones, LR et al. (2003). “The nature and space density of fossil groups of galaxies”. In: *Monthly Notices of the Royal Astronomical Society* 343.2, pp. 627–638.
- Khosroshahi, Habib G, Laurence R Jones, Trevor J Ponman (2004). “An old galaxy group: Chandra X-ray observations of the nearby fossil group NGC 6482”. In: *Monthly Notices of the Royal Astronomical Society* 349.4, pp. 1240–1250.
- Kuntz, KD, SL Snowden (2008). “The EPIC-MOS particle-induced background spectra”. In: *Astronomy & Astrophysics* 478.2, pp. 575–596.
- La Barbera, F et al. (2009). “The Nature of Fossil Galaxy Groups: Are They Really Fossils?” In: *The Astronomical Journal* 137.4, p. 3942.
- Lovisari, Lorenzo et al. (2021). “Scaling properties of galaxy groups”. In: *Universe* 7.5, p. 139.
- Mason, KO et al. (2001). “The XMM-Newton optical/UV monitor telescope”. In: *Astronomy & Astrophysics* 365.1, pp. L36–L44.
- Mernier, F et al. (2018). “Enrichment of the hot intracluster medium: observations”. In: *Space Science Reviews* 214.8, pp. 1–40.
- Mernier, François, Veronica Biffi (2022). “Chemical enrichment in groups and clusters”. In: *arXiv preprint arXiv:2202.07097*.
- Mernier, François, Jelle de Plaa, et al. (2017). “Radial metal abundance profiles in the intra-cluster medium of cool-core galaxy clusters, groups, and ellipticals”. In: *Astronomy & Astrophysics* 603, A80.
- Mewe, R, JR Lemen, GHJ Van den Oord (1986). “Calculated X-radiation from optically thin plasmas. VI-Improved calculations for continuum emission and approximation

- formulae for nonrelativistic average Gaunt factors”. In: *Astronomy and Astrophysics Supplement Series* 65, pp. 511–536.
- Mitchell, RJ et al. (1976). “Ariel 5 observations of the X-ray spectrum of the Perseus Cluster”. In: *Monthly Notices of the Royal Astronomical Society* 175.1, 29P–34P.
- Mulchaey, John S (2000). “X-ray properties of groups of galaxies”. In: *Annual Review of Astronomy and Astrophysics* 38.1, pp. 289–335.
- NASA, *Local Hot Bubble* (n.d.). [https://science.nasa.gov/science-red/s3fs-public/styles/large/public/mnt/medialibrary/2003/01/06/06jan\\_bubble\\_resources/bubble\\_pdf\\_med.jpg?itok=t-Gs\\_jjJ](https://science.nasa.gov/science-red/s3fs-public/styles/large/public/mnt/medialibrary/2003/01/06/06jan_bubble_resources/bubble_pdf_med.jpg?itok=t-Gs_jjJ). [Online]; Available: [Accessed: 05-Feb-2023].
- NED: *NASA/IPAC Extragalactic Database* (n.d.). <http://ned.ipac.caltech.edu>. [Online]; Available: [Accessed: 05-Feb-2023].
- Nolthenius, Richard, Simon DM White (1987). “Groups of galaxies in the CfA survey and in cold dark matter universes”. In: *Monthly Notices of the Royal Astronomical Society* 225.3, pp. 505–530.
- NXSA: *XMM-Newton Science Archive* (n.d.). <http://nxsa.esac.esa.int/nxsa-web/#home>. [Online]; Available: [Accessed: 05-Feb-2023].
- Ponman, Trevor J, Damian B Cannon, Julio F Navarro (1999). “The thermal imprint of galaxy formation on X-ray clusters”. In: *Nature* 397.6715, pp. 135–137.
- Sanderson, Alastair JR et al. (2003). “The Birmingham—CfA cluster scaling project—I. Gas fraction and the M—TX relation”. In: *Monthly Notices of the Royal Astronomical Society* 340.3, pp. 989–1010.
- Sarazin, Craig L (1988). “X-ray Emission from Clusters of Galaxies”. In.
- Sarkar, Arnab et al. (2022). “Chemical abundances in the outskirts of nearby galaxy groups measured with joint Suzaku and Chandra observations”. In: *Monthly Notices of the Royal Astronomical Society* 516.2, pp. 3068–3081.
- Sato, Kosuke et al. (2010). “Metallicity of the Fossil Group NGC 1550 Observed with Suzaku”. In: *Publications of the Astronomical Society of Japan* 62.6, pp. 1445–1454.
- Smith, Randall K et al. (2001). “Collisional plasma models with APEC/APED: emission-line diagnostics of hydrogen-like and helium-like ions”. In: *The Astrophysical Journal* 556.2, p. L91.
- Snowden, SL, MR Collier, KD Kuntz (2004). “XMM-Newton observation of solar wind charge exchange emission”. In: *The Astrophysical Journal* 610.2, p. 1182.
- Snowden, SL, KD Kuntz (2014). *Cookbook for analysis procedures for XMM-Newton EPIC observations of extended objects and the diffuse background*.
- Snowden, SL, RF Mushotzky, et al. (2008). “A catalog of galaxy clusters observed by XMM-Newton”. In: *Astronomy & Astrophysics* 478.2, pp. 615–658.
- Strüder, L et al. (2001). “The European photon imaging camera on XMM-Newton: the pn-CCD camera”. In: *Astronomy & Astrophysics* 365.1, pp. L18–L26.
- Sun, Ming (2012). “Hot gas in galaxy groups: recent observations”. In: *New Journal of Physics* 14.4, p. 045004.
- Turatto, Massimo (2003). “Classification of supernovae”. In: *Supernovae and Gamma-Ray Bursters*. Springer, pp. 21–36.
- Turner, Martin JL et al. (2001). “The European photon imaging camera on XMM-Newton: the MOS cameras”. In: *Astronomy & Astrophysics* 365.1, pp. L27–L35.
- Voit, G Mark (2005). “Tracing cosmic evolution with clusters of galaxies”. In: *Reviews of Modern Physics* 77.1, p. 207.

Woosley, Stan, Thomas Janka (2005). “The physics of core-collapse supernovae”. In: *Nature Physics* 1.3, pp. 147–154.

*XSPEC TCL Scripting Documentation* (n.d.). <https://heasarc.gsfc.nasa.gov/xanadu/xspec/xspec11/tcl/tcl.html>. [Online]; Available: [Accessed: 05-Feb-2023].